Stony Brook University

OFFICIAL COPY

CHARACTERISTICS OF COHERENT FIBER OPITCS IMAGING

BUNDLE AFTER HIGH POWER TRANSMISSION

A Thesis Presented

By

Shih Hsi Yen

To

The Graduate School

in Partial Fulfillment of the

Requirements

for the Degree of

Master of Science

in

Electrical Engineering

Stony Brook University

December 2010

STONY BROOK UNIVERSITY

THE GRADUATE SCHOOL

<u>Shih Hsi Yen</u>

We the thesis committee for the above candidate for the
Master of Science degree,
hereby recommend acceptance of this thesis

Harbans S. Dhadwal, Advisor of Thesis
Associate Professor, Department of Electrical and Computer Engineering

Murali Subbarao,
Professor, Department of Electrical and Computer Engineering

This thesis is accepted by the Graduate School

Lawrence Martin
Dean of the Graduate School

Abstract of the Thesis

Characteristics of Coherent Fiber Optics Imaging Bundle

After

High Power Transmission

by

Shih Hsi Yen

Master of Science

in

Electrical Engineering

Stony Brook University

2010

This thesis presents a comparative experimental characterization of a coherent fiber optics imaging bundle or coherent fiber bundle (CFB) before and after exposure to high energy density pulses ($> 1k$ J/cm^2). A Fujikura FIGH-30-850N ultra-thin imaging fiber with 30,000 individual optical fiber filaments, packed into a 780 μm spot, was selected and tested. Two fiber-coupled laser diodes, operating at a wavelength of 818 nm and 830nm respectively, provided the high power excitation source for the experiments. Precise control of the incident energy density was achieved through a combination of current regulation and pulse width control. The latter

technique enabled a pulse-width range from 50 ms to continuous wave (CW) operation at constant repetition rate of one second (1 Hz). The transmitted image through the CFB was observed with an Olympus BH-2 Microscope and recorded with a 2 Megapixel digital microscope still image camera, μCapture.

Post processing of the recorded image was done using software tools, such as, ImageJ (Image Processing and Analysis in JAVA) and MATLAB (MATrix LABoratory). Analysis done using visual inspection and modulation transfer function techniques revealed that the laser induced fiber damage threshold (LIFDT) of the CFB is greater than 11k J/cm^2. This high damage threshold is much larger than the accepted levels used for diverse medical procedures, such as, photoepilation. The results indicate that CFBs can be used for precise delivery of lethal doses of optical energy needed to destroy unwanted tissues, in addition to transporting images from remote locations. Through experiments, the results ensure the practicability of using CFB for both imaging and power transmission for the many diverse applications using photoinduced therapies.

To

My Parents

For their continuous support, encouragement and patience

And

In the memory of my grandparents

TABLE OF CONTENTS

LIST OF FIGURES

LIST OF TABLES

ACKNOWLEDGEMENTS

1.0 Introduction

The use of coherent fiber bundles (CFB) for transporting images of inaccessible objects can be traced to the pre-communication era [1], which represents the genesis of fiber optics. The early systems, despite being years ahead of the accompanying technologies laid the foundation of imaging through a CFB. Today, CFBs are prevalent in wide variety of industries, ranging from machine vision to fiberscope, with health care being the dominant. Use of CFBs in endoscopes produces a powerful diagnostic tool for visual exploration of various human anatomical features. For example, colonoscopy is a very valuable procedure for early detection of colon cancer. Bronchoscope allows the physician to explore obstruction in the upper respiratory system. Gastroscope, the original inspiration for the development of fiber optics, is used to peek inside the stomach. These applications are primarily passive, as the CFBs record the image of remote objects. Typically, additional fibers are introduced for illumination of the object field.

Endoscopes may include the use of incision instruments which allow physicians to perform key-hole surgery. Other types include the use of separate high power transmission, metal coated hollow fibers for laser induced damage to tissue, for closing small blood vessels to reduce blood loss or removing tumors during surgery. In all the above applications, the CFB is used for image transport only. This thesis explores the possibility of using the CFB for the transmission of high energy optical pulses, in addition to the image transport. This dual use of CFBs has the potential for more compact endoscopes.

A trend of new generation laser hair removal devices for home usage is at rise according to a medical paper published in Elsevier [9]. In 2007, 11.7 million cosmetic surgical and nonsurgical procedures were performed in the United States, with laser hair removal being the

third most common nonsurgical procedure, accounting for 1,412,657 visits [9]. Women

accounted for 87% of these hair removal procedures, with laser hair removal being the most

common nonsurgical cosmetic procedure for individuals between ages of 19 to 34 years. The

hair removal industry is approximately 10 billion dollars annually, and many companies are

eager to tap into this market with new and exciting products. While now more manufactures have

shifted towards making devices more user friendly, most laser hair removal procedures are still

performed using large, expensive devices in medical facilities by trained physicians. We are

targeting the device for non-medical facilities with minimally trained staff and for educated users

in a home-based environment.

Photoepilation is based on sound principles of photothermolysis for the destruction of

cellular structures in the hair follicle for prevention of re-growth. Photoepilation with laser

pulsing techniques at a wavelength approximately between 650 nm to 1100 nm is proven to

successfully provide long term management of hair removal for both men and women [9].

Complications arising after hair removal are being minimized through a deeper understanding of

the mechanisms involved. Typically, fluence requirement is in the range of 1 J/cm^2 to 1000 J/cm^2

depending on the selected pulse width (millisecond range).

Figure 1.1 briefly illustrates the use of CFB for a compact photoepilation system [2]. The

image of the object is de-magnified by a fiber mounted lens into the distal end of the CFB. This

image is transported through a CFB (having a diameter of approximately 1 mm) to the other side

without changing the orientation. On the proximal end, the image and transmission paths are

separated by a beam splitter and a notch filter. Separate lenses insure independent optical

conditions can be attained for the transmission of high energy pulses and the recording of the

image by the CCD camera. A notch filter centered at the frequency of the laser is installed in

front of the camera to ensure the reflected laser pulses are blocked and do not pass through into the sensor of the camera and damage it during transmission.
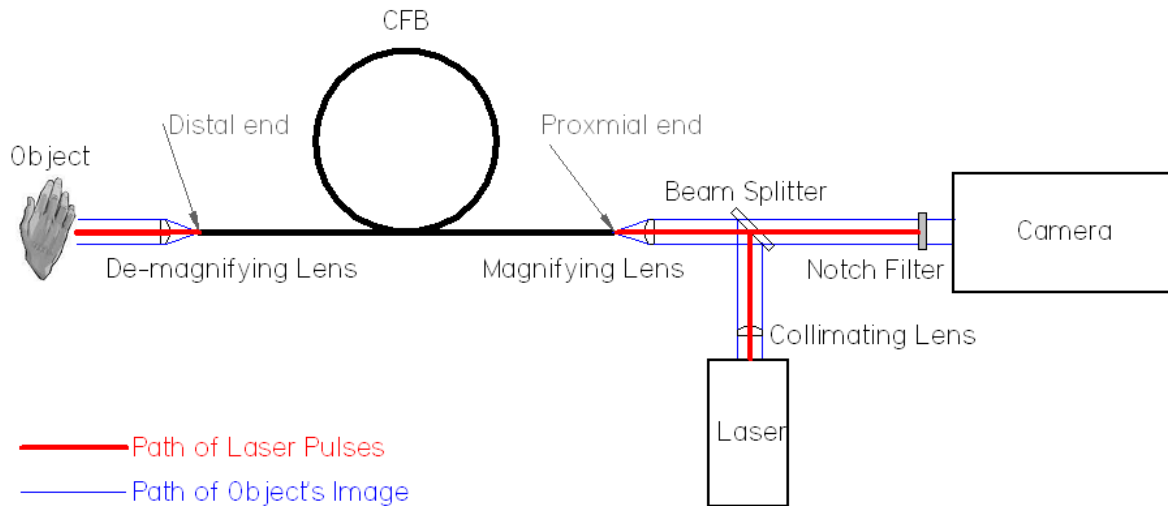
Figure 1.1 Design of a compact photoepilation system

The main objective of this thesis report is to examine the characteristics of the CFB before and after transmission of high energy density laser pulses in various power settings, thereby gaining some insight into whether the system described in Figure 1.1 can be realized. Through post image processing analysis with visual inspection and modulation transfer function techniques, a laser induced fiber damage threshold (LIFDT) could be established for a Fujikura FIGH-30-850N CFB.

3

2.0   Theoretical Background

A CFB is made of tens of thousands of fibers drawn together. Depending on the size and the resolution of a CFB, each individual fiber in a bundle can range from 2 to 20 μm in diameter. In the case of Fujikura FIGH-30-850N each individual fiber is approximately 2μm in diameter, which is the highest resolution the manufacture offers. However, the shape and diameter of individual fibers is intentionally distributed over a narrow range, in addition to the random spacing. This deliberate asymmetry minimizes the cross-coupling between neighboring fibers.

There are two basic families of fiber bundles: 1) a rigid fiber bundle; 2) a thin flexible fiber bundle [3]. A rigid fiber bundle is constructed by fusing individual fibers together to make a solid block. It retains the light-guiding property of the individual fibers that are aligned end to end in the bundle. A rigid fiber bundle, typically short and fat, is used as an optical device for transmitting and de-/magnifying images piece by piece [3]. A flexible fiber bundle is used for transporting images from inaccessible places [3]. There are two kind of flexible fiber bundles in this family: coherent fiber bundle (CFB) and incoherent fiber bundle (IOFB). The latter is primarily used for transporting light to inaccessible places, for the purpose of providing illumination. In combination with photo-voltaic cells it can provide a source of energy for hazardous or inaccessible environments.

A CFB, sometimes called an ordered bundle, is used as an imaging conduit [4]. Each optical fiber is accurately aligned in an ordered bundle, such that an image incident on one end is faithfully transported to the other end. As illustrated in Figure 2.1, the alphabet character "A" is transported from the proximal end to the distal end.

4
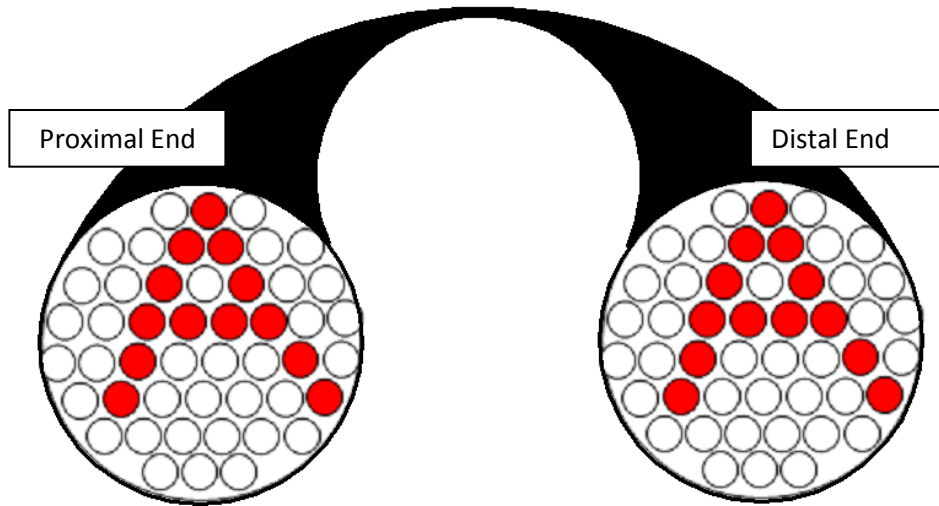
Figure 2.1 Letter "A" transports through a Coherent Fiber Bundle

IOFB is sometimes referred as non-ordered bundle [4]. As name suggests, non-ordered bundle does not have spatial correspondence from one end of the fiber to the other; therefore, it is mainly used for illumination purpose. As illustrated in Figure 2.2, incoherent fiber bundle does not transport the "A" from proximal end to distal end; the illuminated fibers at the distal end have been randomly shuffled.
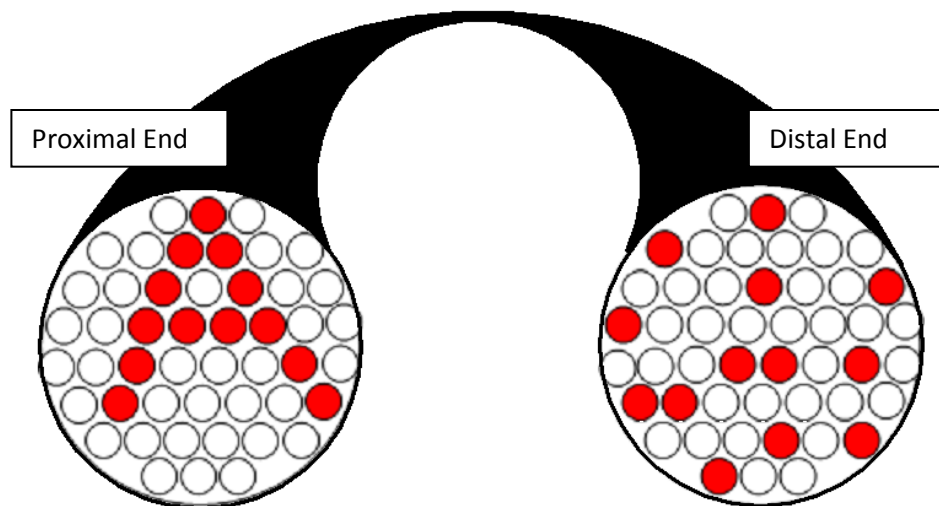
Figure 2.2 Letter "A" transports through an Incoherent Fiber Bundle

Due to high price tag and restriction on the length of CFB, engineers have tried to use IOFB for transporting images. Studies show that an IOFB can indeed transport images by post-processing the information carried by each individual fibers and correlating them digitally to achieve the proximate position as aligned in the distal end [8]. However, since the resolution of post-processed IOFB is inferior to CFB, we will not investigate it further in this thesis.

2.1 Modulation Transfer Function

Modulation Transfer Function (MTF) or spatial frequency response is commonly used to test the performance of an optical imaging system [5]. MTF, a quantitative measure of image quality, is expressed as a ratio of the image to object contrasts at a particular spatial frequency. However, practical standardized MTF chart consists of a series of alternating light and dark bands in equal or varying width and are readily available for characterizing new design. At a particular spatial frequency the modulation index, M, is given by,

$$M = \frac{n_{max} - n_{min}}{n_{max} + n_{min}} \tag{2.1}$$

where n_{max} and n_{min} represent the maximum and minimum brightness levels or gray levels of the image. If the contrast of an image is expressed as a modulation given by the equation, we can plot the modulation as a function of the number of lines per millimeter in the image [5]. The MTF is the ratio of the modulation in the image to that in the object as a function of the frequency (v, cycles per unit of length) of the wave pattern described in Equation (2.2) [5].

$$MTF(v) = \frac{M_i}{M_o} \tag{2.2}$$

By ordering the frequency of the modulation sequentially, the spatial frequency response of the image is obtained.

If we assume an object consisting of alternating light and dark bands, the brightness of which varies according to a cosine function, the spatial distribution of light can be expressed mathematically by

$$G(x) = b_0 + b_1 \cos(2\pi v x) \qquad (2.3)$$

where v is the frequency of the brightness variation in cycles per unit length, $(b_0 + b_1)$ is the maximum brightness, $(b_0 - b_1)$ is the minimum brightness, and x is the spatial coordinate perpendicular to the bands [5]. The modulation of this pattern is expressed by

$$M_o = \frac{(b_0 + b_1) - (b_0 - b_1)}{(b_0 + b_1) + (b_0 - b_1)} = \frac{b_1}{b_0} \qquad (2.4)$$

M_i, the modulation of the transported image, is determined in the same approach as M_o. With both M_o and M_i, MTF can be constructed as described in Equation (2.2).

The USAF 1951 lens test chart, Figure 2.3, and its variants have been an accepted standard for characterizing optical systems. Recently, founder and CTO of Imatest suggested that the chart was inappropriate for computer analysis and it was poorly suited for visually estimating the MTF.
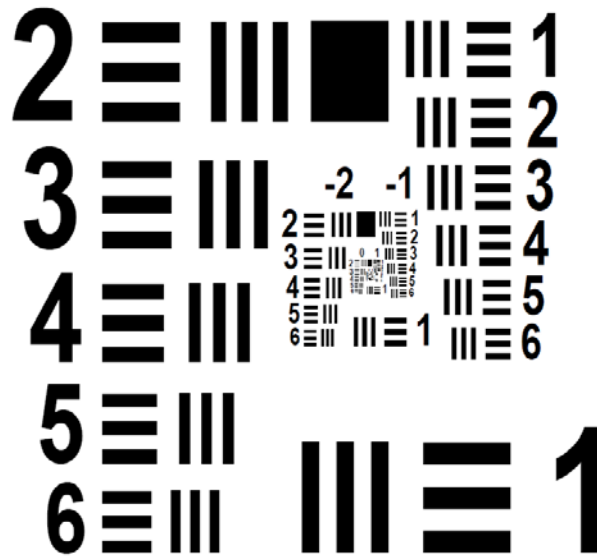
Figure 2.3 The USAF 1951 lens test chart (visual inspection only)

He argues that the alternating bars are not arranged linearly which can be problematic for computer analysis, and estimating MTF visually can be subjective and unreliable. He constructed the Koren 2003 lens tests chart, shown in Figure 2.4, whose recorded image can be analyzed using the combination of ImageJ and MATLAB program [10].
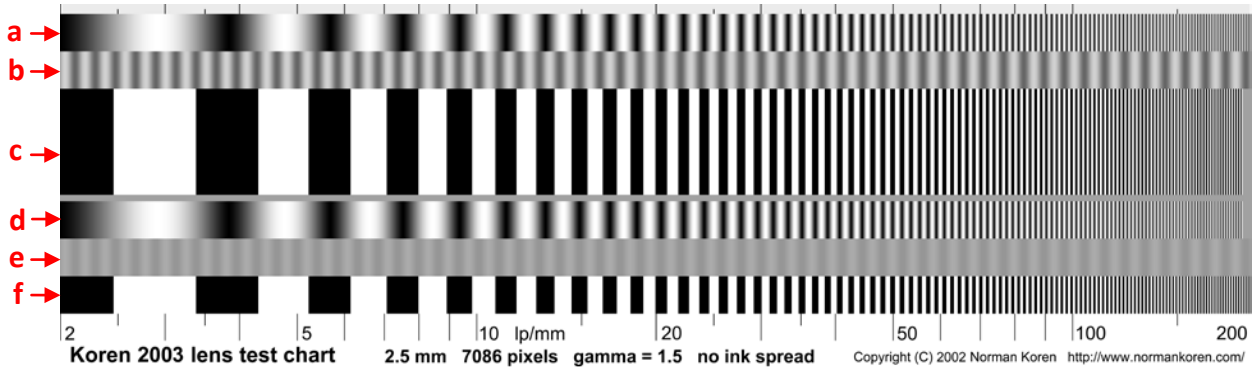
Figure 2.4 The Koren 2003 lens test chart (analyzable by computer) (a)&(d) Sine pattern, 2-200 lp/mm, for determining MFT response; (b) 50% contrast reference; (c)&(f) Bar pattern, 2-200 lp/mm, for visual estimation of sharpness; (e) 10% contrast reference;

The spatial frequency of Koren 2003 lens test chart increases continuously from 2 to 200 line pairs per millimeter (lp/mm) on a logarithmic scale. It includes a sine pattern for estimating MTF response, a bar pattern for visually estimating sharpness, and contrast reference patterns for visually evaluating film image of the chart. The length of the Koren 2003 lens test chart is 25 cm long which is printable to an A4 paper. The chart is designed to be imaged 100 times smaller, at 2.5 mm long.

In the MTF of the Data Analysis section, the sine wave of the Koren 2003 lens test chart was chosen for calculating the MTF of our optical system for each experiment. Norman Koren's sampled analysis routine with ImageJ and MATLAB code [10] was also borrowed to evaluate our system.

3.0 Hardware Implementation and Setup

Two experimental units were designed for this thesis research: Fiber Damaging Unit (FDU) and Fiber Analyzing Unit (FAU). FDU provides controlled fluence of the laser pulses fired into the proximal end of the CFB. A FAU is an optical system for capturing images and identifying any anomalies or damages on the CFB after the FDU stage.

3.1 Fiber Damaging Unit

In order to determine if the CFB is suitable for delivering high power and high density monochromatic laser pulses, a series of tests were undertaken to find the LIFDT. Figure 3.1 below illustrates a basic block diagram for the Fiber Damaging Unit and Figure 3.2 is a photograph of the actual system.

Fiber Damaging Unit
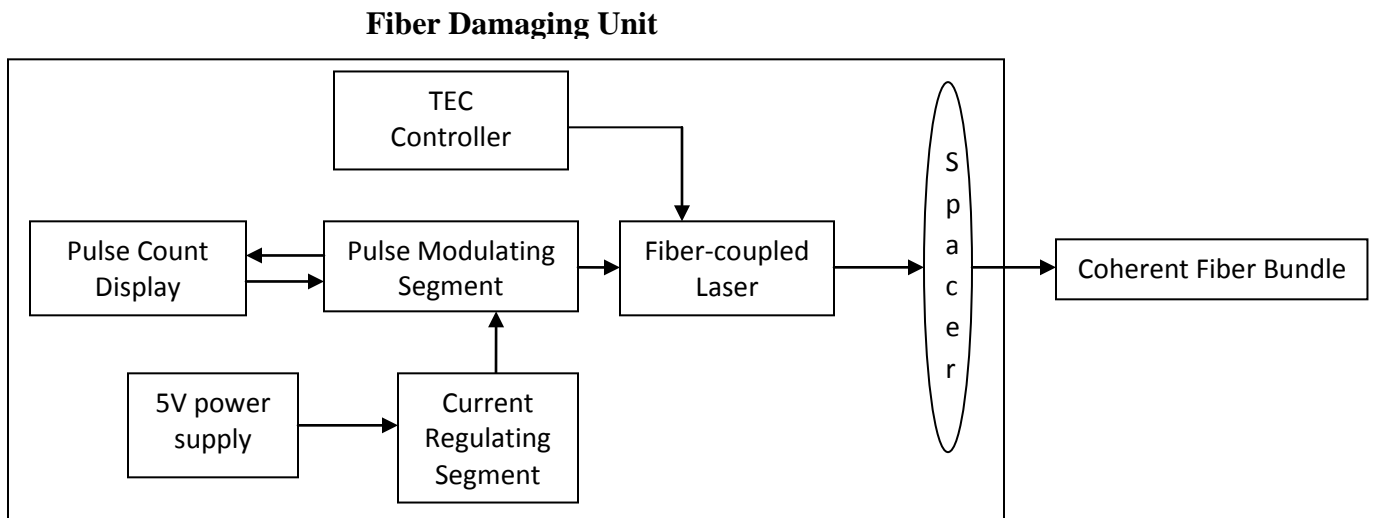
Figure 3.1 Fiber Damaging Unit Block Diagram
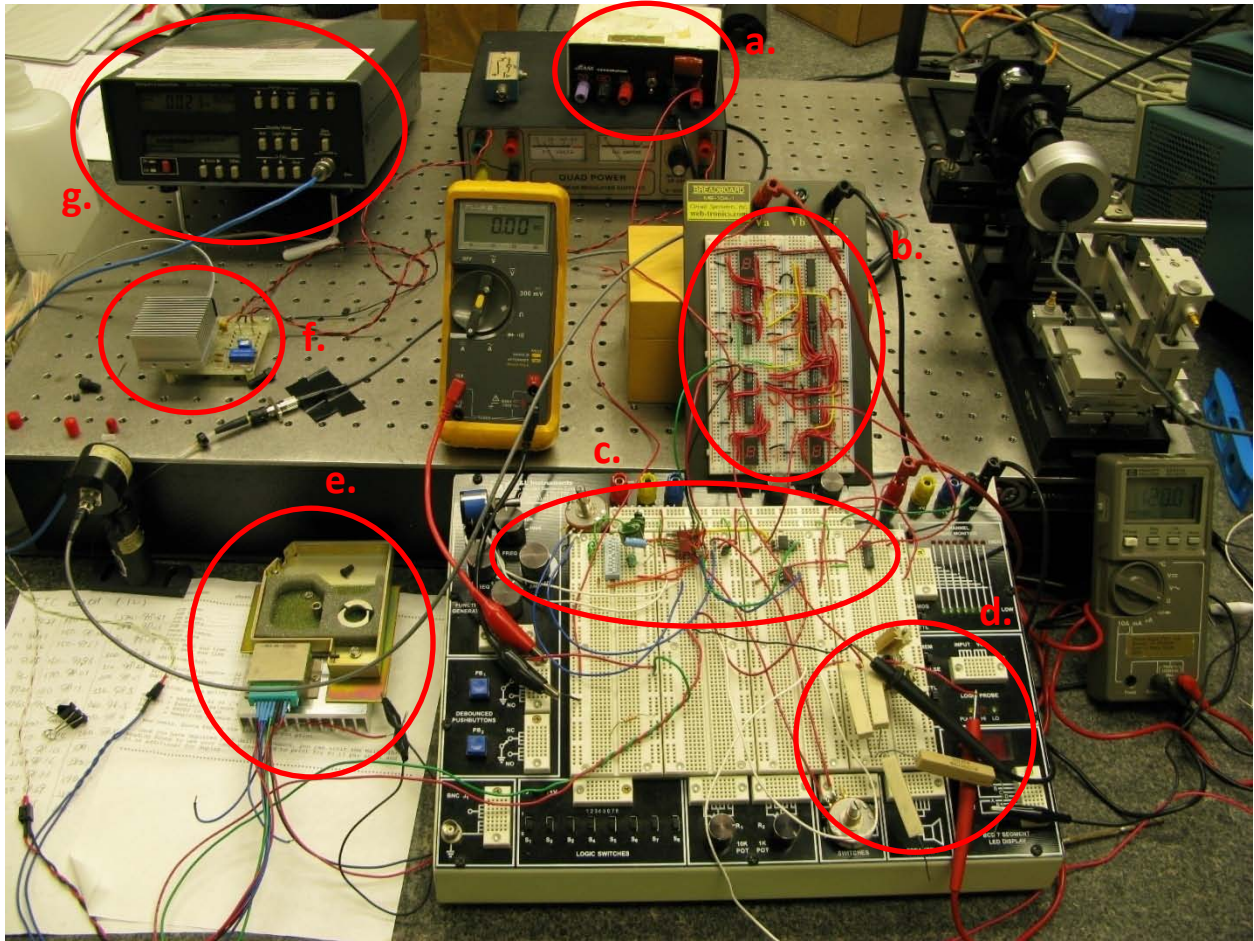
Figure 3.2 Picture of the actual system setup of Fiber Damaging Unit. (a) 5 volt power supply (able to deliver up to 3 ampere); (b) Pulse Count Display; (c) Pulse Modulating Segment; (d) Current Regulating Segment; (e) fiber-coupled laser module; (f) TEC Controller; (g) power meter;

3.1.1   TEC Controller

The output power of laser diode is temperature dependent. When constant current is applied to a laser diode, the increase in temperature will causes the output power to decrease. To avoid output power fluctuation, most laser diodes have either or both the built-in thermistor and thermoelectric cooler (TEC), or a bulky heat sink to dissipate the heat generated during its operation.

In our experiments the HY-5610, made by Hytek Microsystems, was used to control the in-built TEC of the laser module. The HY-5610 is a subminiature proportional temperature

controller for the TEC [6]. This device is intended for "heat or cool" of fixed temperature

applications. Therefore, when the temperature of the thermistor is lower than the set temperature

or higher than the set temperature, the HY-5610 will control the TEC to heat or cool

respectively. In laboratory environment, the laser module needs to be cooled only. The HY-5610

uses a thermistor bridge to precisely measure and regulate the temperature of the laser module

affixed to the TEC. There is a Temperature Set Resistor which controls the temperature at which

the TEC will operate. When the circuit has stabilized, the resistance of the thermistor will be

equal to that of the set resistor Rs.

Referring to the Thermistor Resistance versus Temperature Chart in Appendix A, we

were guided to choose the Rs to be 12.14 kΩ for the Laser to be maintained at 21 $^{\circ}$C. This value

allows the Laser module to operate normally.

3.1.2 Current Regulating Segment

Laser diode is sensitive to current fluctuation; therefore, current must be closely

monitored and regulated at all times. A LM317, 3- Terminal Positive Adjustable Regulator, from

Fairchild Semiconductor is used in constant current mode to prevent thermal runaway in the

system. Thermal runaway in our case would most likely be caused by an overpowered resistor.

The cycle begins with a decreasing resistance as the overpowered resistor heats up and due to

reduce in resistance, the current in the circuit will increase. Eventually, the laser diode current

will exceed the safe operational threshold, resulting in catastrophic failure of the diode. A

gradual failure may go undetected, resulting in sub-optimal performance of the instrument over

an extended period of usage. A schematic of the current regulating circuit is shown in Figure 3.3.

By adjusting the resistor R_{11}, current passing through the laser diode can be varied and regulated.

In order to prevent resistor, R_{11}, from heating, power across R_{11} must be within its power rating range.
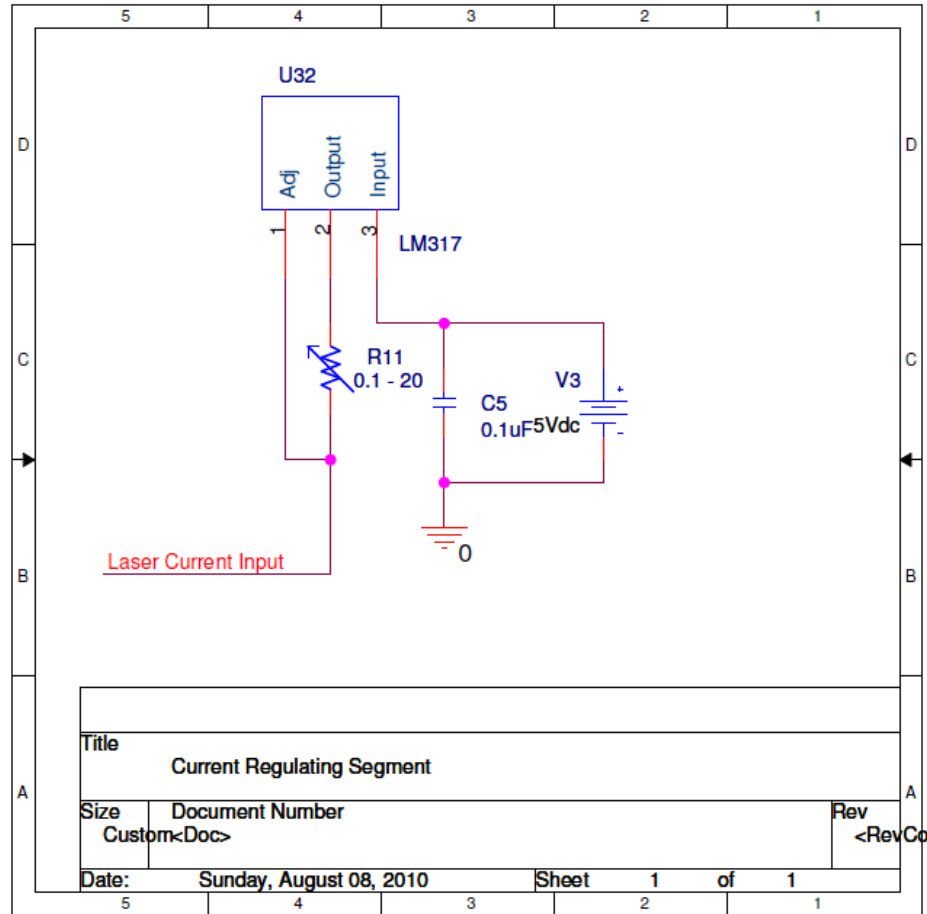
Figure 3.3 Current Regulating Segment

3.1.3 Pulse Modulating Segment

The output power of the laser module can be manipulated with the current regulating segment alone, however, a preferred method uses pulse width modulation. The latter allows better control of the pulse energy and it is directly applicable to established hair removal protocols [7]. Typically, the laser pulse width must be adjusted to match the Thermal Damage

Time. In addition to pulse width control, the study of LIFDT requires precise counting of the number of pulses.

The pulse modulating segment, shown in Figure 3.4, contains a 555 timer, two optically coupled MOSFETs, a positive-edge triggered D Flip-Flop and a switch. The 555 timer, NE555P made by Texas Instrument, generates and controls the pulse width (τ_w) and period (T) of the output signal. Equation (3.1) explains how varying the duty cycle of the output signal changes the output power (P_{out}) that the system can deliver. For the experiment, a constant pulse period of 1 second was maintained. Pulse width can vary from minimum of 2 ms to a full period or CW operation.

$$P_{out} = P_{in} \times Duty\ Cycle = P_{in} \times \tau_w/T \tag{3.1}$$

An optical-coupled MOSFET, PS710A made by California Eastern Laboratories has a maximum current rating of 3.6A, which is more than sufficient for driving the Laser module. However, the speed and differential delay between the turn-on (1 ms) and turn-off (0.05 ms) times are more critical to the use of the pulse width modulation circuit. Tests revealed a delay of 1.05 ms in rise time and 85 μs in fall time of a pulse propagating through the MOSFET. Consideration of these delays imposed a practical limit of 10 ms on the minimum pulse width that could be used.

The output signal of the 555 timer drives the anode of internal LED of the first optical-coupled MOSFET. A grounded current limiting resistor was installed after LED cathode to prevent over-driving the LED. As the LED turns on and off with respect to the signal from the 555 timer, the MOSFET turns ON and OFF thereby controlling the amount of current flowing through the laser diode.

The second optical-coupled MOSFET was implemented to turn off the laser module once the desired pulse count was reached. This was realized by introducing a positive-edge triggered D Flip-Flop, DM74LS74A by National Semiconductor. Pulse output from the 555 timer is connected to the clock pin of the DM74LS74A. The pulse counter, which is chosen from one of the three 7-segment displays for desired pulse count, is connected to the D pin of the Flip-Flop. The LED anode of the second MOSFET is tied to inverse Q; therefore, as long as the pulse count has not been achieved the output of the D Flip-Flop remains high. When the pulse count reaches its set target, the MOSFET turns off.

A manual, hard switch was implemented between the source of the first MOSFET and the drain of second MOSFET to prevent the laser from pulsing again. When the pulse count has been achieved, the user has sufficient time to turn off the hard switch without worrying about the introduction of stray pulses. For example, if the desired pulse count is 20, the user has an additional 20 seconds before the laser starts pulsing again. In the case of using a full period pulse or CW, the pulse modulating segment will be bypassed and current regulating segment will connect directly to the laser module to drive the laser diode.
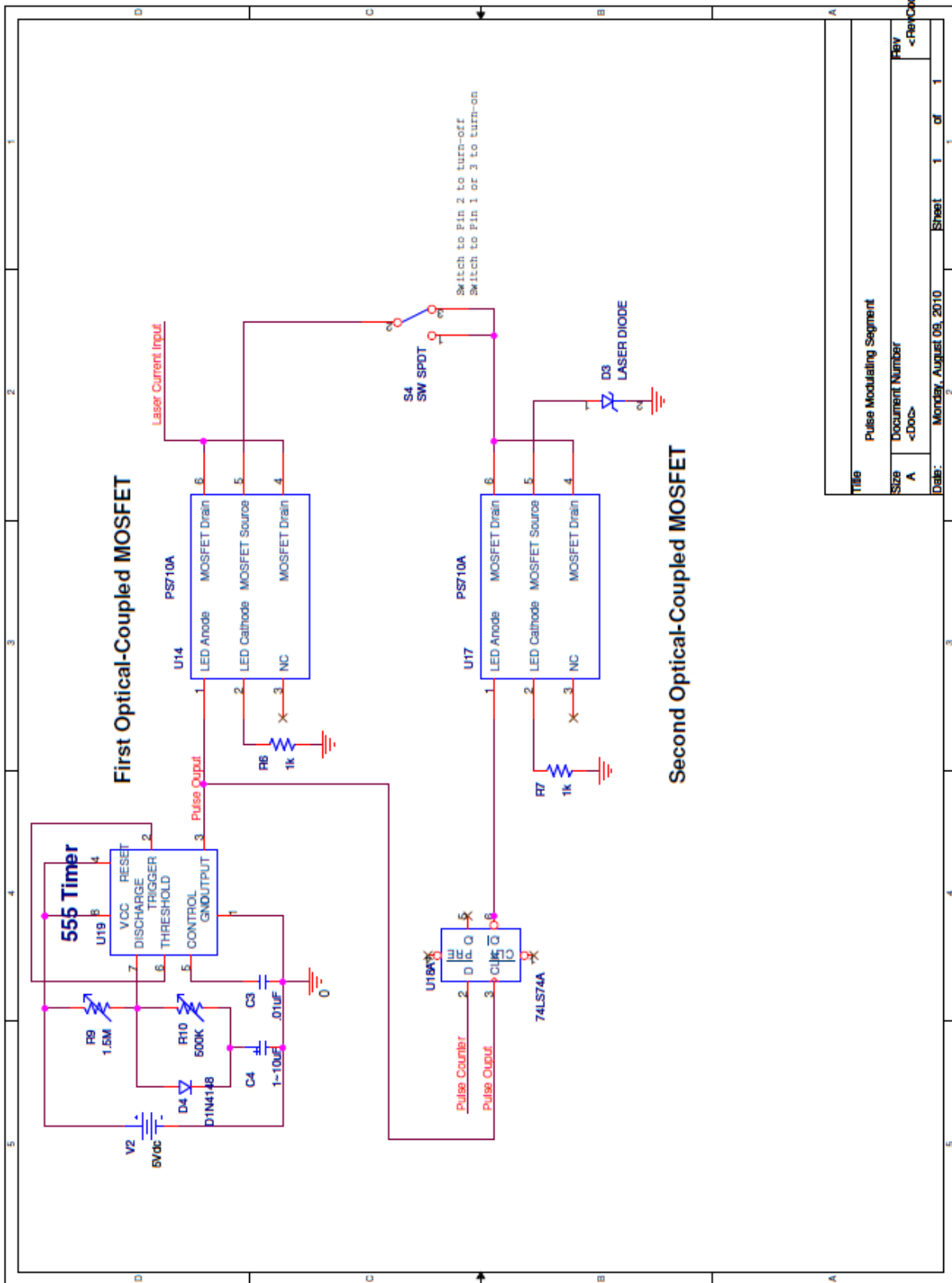
Figure 3.4 Pulse Modulating Segment: Variable from 10ms to full period

3.1.4 Pulse Count Display

Three seven segment displaying units are deployed in the Pulse Count Display circuit of Figure 3.5. The first seven segment displaying unit is constructed with a decade and binary counter, a BCD to seven segment decoder, a seven segment display, half of Quad 2-Input NOR Gate IC and one gate from the Quad 2-Input AND Gates IC. The decade counter (BCD counter), DM74LS74N made by National Semiconductor, is connected to a BCD to seven segment decoder, SN74LS48N made by Motorola, to display on a seven segment display. The four output pins from the BCD counter are also tied to an AND gate and a NOR gate for detecting counter value "1001". The second AND gate is used for checking these two gates. When counter value "1001" is detected, both AND gate and NOR gate will output one, and thereby the second AND gate will also be outputting a one. This signal is passed on to the second seven segment display as the clock signal of the new BCD counter. The second and third seven segment displaying units are constructed identical to the first one, except that the third seven segment displaying unit does not require AND and NOR gates for further counting.

The number of pulses are counted and displayed on the seven segment displays start from bottom left to top right as demonstrated in the actual system in Figure 3.2. The count starts from an initial state of "000" to a maximum count of "999"; it returns to "000" thereafter. The desired pulse count is set by choosing one of the BCD counter values and wiring it to the D Flip-Flop in Pulse Modulating Segment to stop the laser diode from pulsing once the counts have been complete.
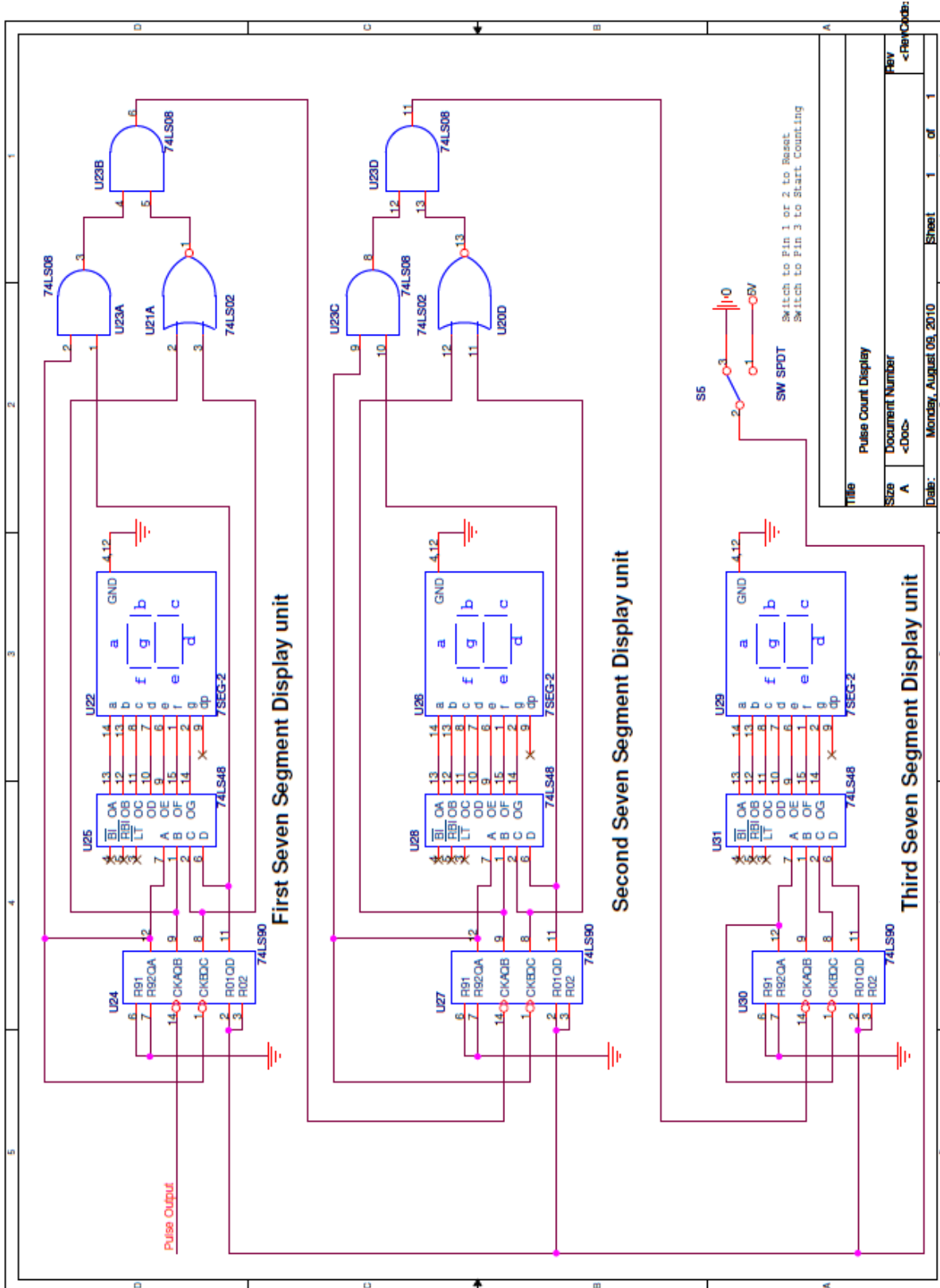
Figure 3.5 Pulse Count Display: three digit decimal counter display

3.1.5 Fiber-coupled Laser

The laser module was salvaged from an old Kodak copier. Unfortunately, the specifications of the Laser diode could not be recovered from the vendor. The laser diode is pigtailed into a 50/125 multimode fiber, Corning infiniCor 600. The fiber has a Numerical Aperture (NA) of 0.200 ± 0.015. The spectral output, Figure 3.6, of the laser diode was characterized by a spectrometer (Ocean Optics, Inc. model # SD 1000). The laser diode has a center wavelength of 818 nm with 28.5-nm-FWHM. The drive current versus output optical power of the laser module is plotted in Figure 3.7.
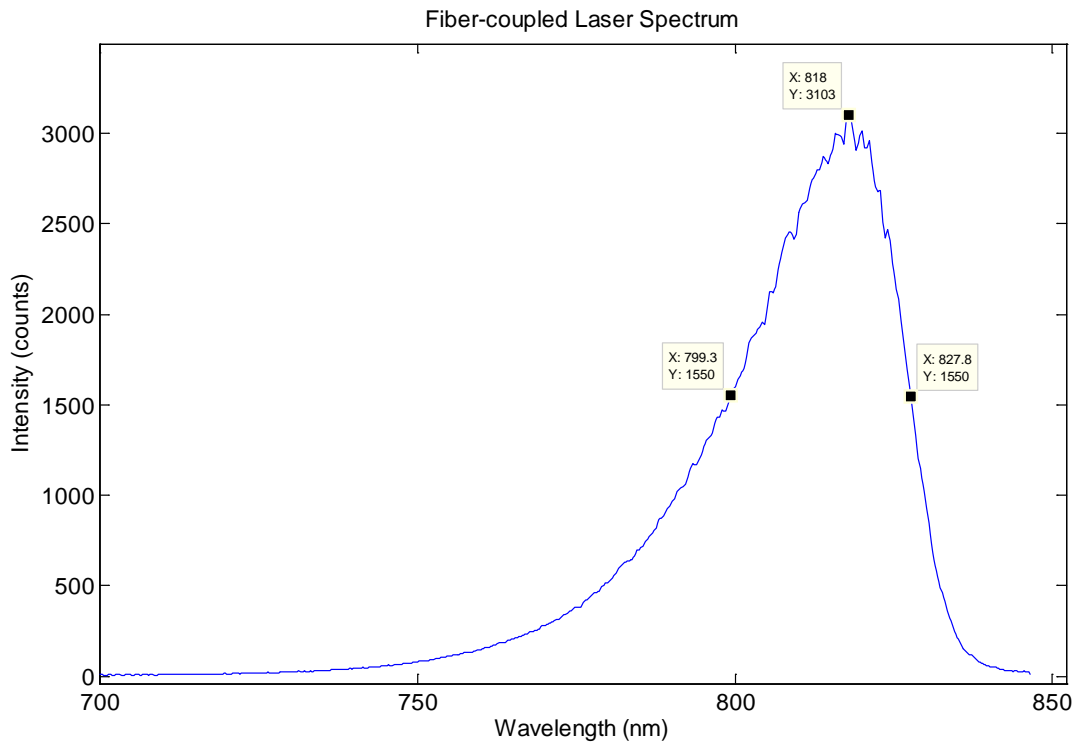
Figure 3.6 The Laser diode Spectrum: centered at 818nm with 28.5-nm-FWHW
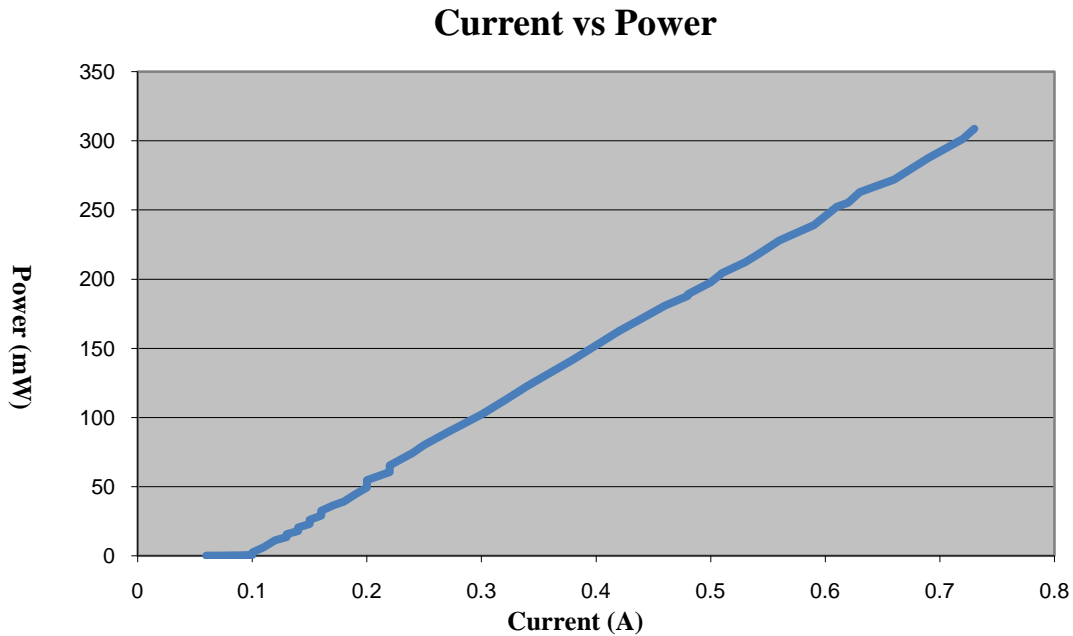
Current vs Power

Figure 3.7 The Laser diode drive current versus output optical power

3.1.6 Coherent Fiber Bundle

A Fujikura FIGH-30-850N, ultra-thin image fiber, was used for the experimental investigations. The fiber contains a nominal of 30,000 individual fiber or picture elements. Each fiber is around 2 µm in diameter and non-uniform in shape to reduce crosstalk between neighboring fibers (shown in Figure 3.8). The diameter of the fiber is approximately 850 micrometer and the image circle, 780 micrometer. To facilitate ease of use and establish efficacy of repeatable measurements, five samples of the CFB were prepared. As shown in the photo in Figure 3.9 short sections of the CFB were mounted into commercial FCPC fiber optic connectors and both ends polished to an optical flatness of $\lambda/25$ using a Buehler fiber optic polisher.
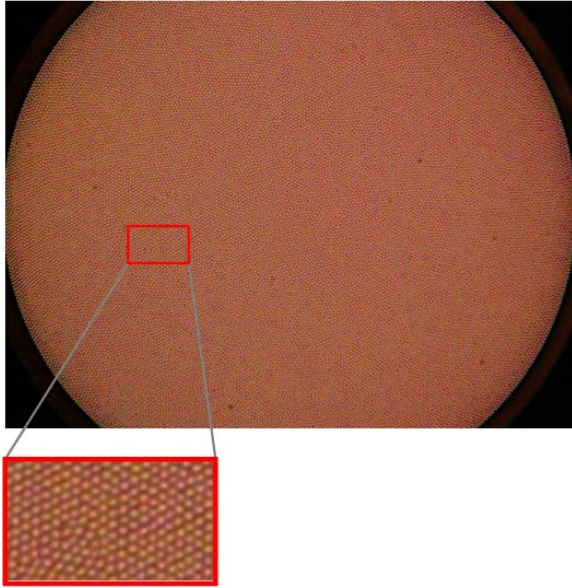
Figure 3.8 Picture of the CFB and the individual fiber elements inside the CFB

Figure 3.9 CFBs mounted in FCPC connectors (Picture taken on a CFB was experimented without a spacer) Top) Proximal end of the CFB (Laser Pulsing end); Bottom) Distal end of the CFB (MFT transporting end);

3.2　Fiber Analyzing Unit

In order to be properly examined the characteristics of the CFB before and after high power and high density pulse transmission, system setup must be robust, systematic and consistent throughout the experiments. Fiber Analyzing Unit was designed to perform repetitive measurements and achieve reliably accurate positioning.

The block diagram for Fiber Analyzing Unit in Figure 3.10 shows the illumination path from both front and bottom light sources and the setup. Figure 3.11 is a photograph of the actual system used.
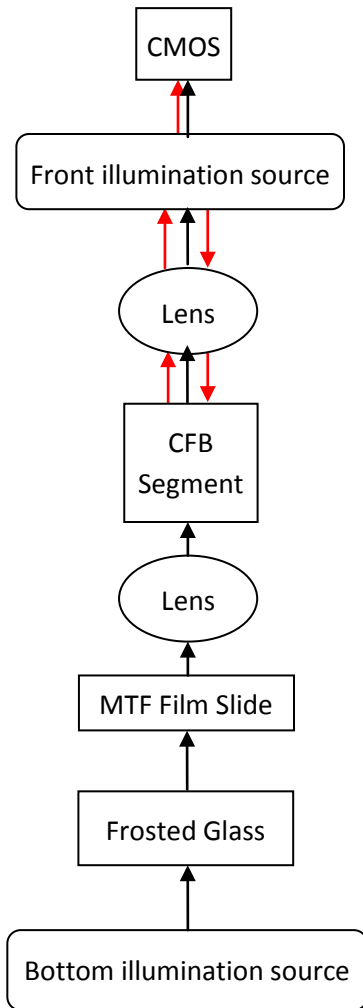
Figure 3.10 Block Diagram for Fiber Analyzing Unit

← ──── Top illumination path to camera
← ──── Bottom illumination path to camera
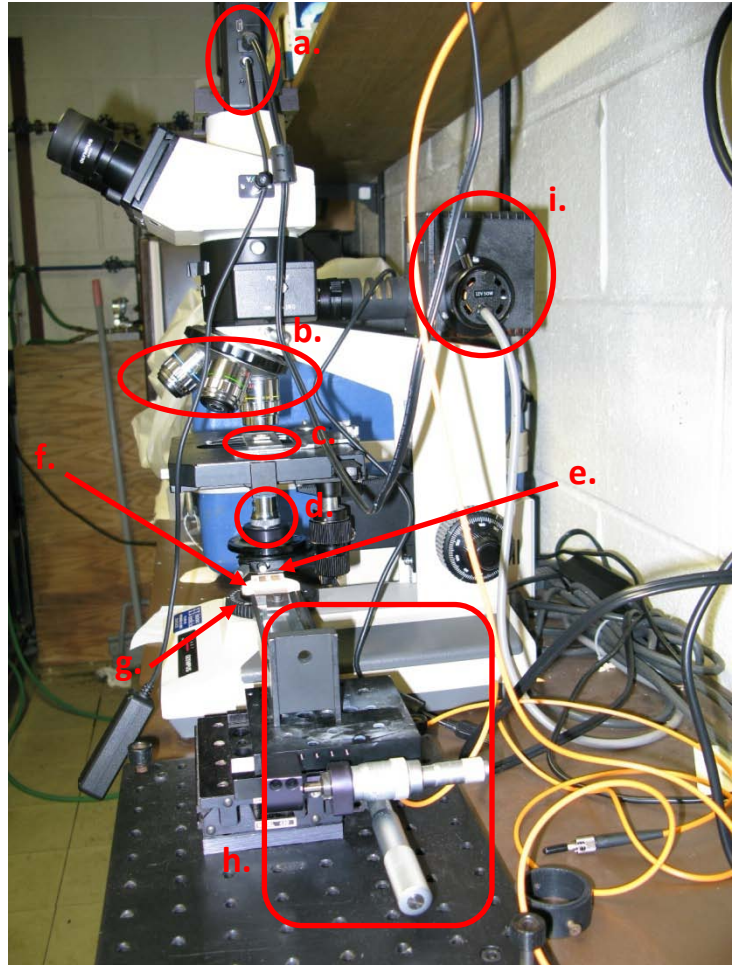
Figure 3.11 Fiber Analyzing Unit
(a) CMOS camera; (b) microscope (10X magnifying) objectives;
(c) CFB Segment and slide; (d) (40X) de-magnifying objectives;
(e) MTF Film slide; (f) frosted glass; (g) back illumination
source; (h) MTF x-y axis stages; (i) front illumination source;

3.2.1   Microscope Digital Camera

µCapture is a specific digital camera for microscope. It has a 2 megapixel CMOS image sensor and offers two functions, one for use as a digital still camera, the other for use as a PC camera. All of the images recorded were taken in still camera mode to achieve maximum resolution. However, since each image had to be manually focused with respect to the image sensor of the camera, PC camera mode was required to view live images projected from the microscope lens.

3.2.2 MTF film stage

The Koren 2003 lens test chart designed by Norman Koren and was photographed and developed into a 35mm Kodak 400TX Black-and-White negative film. The length of the filmed chart was measured 12.51mm and 3.94mm in width. The MTF film, Figure 3.12, is stacked between two glass slides and mounted into a X and Y direction positioning stage.
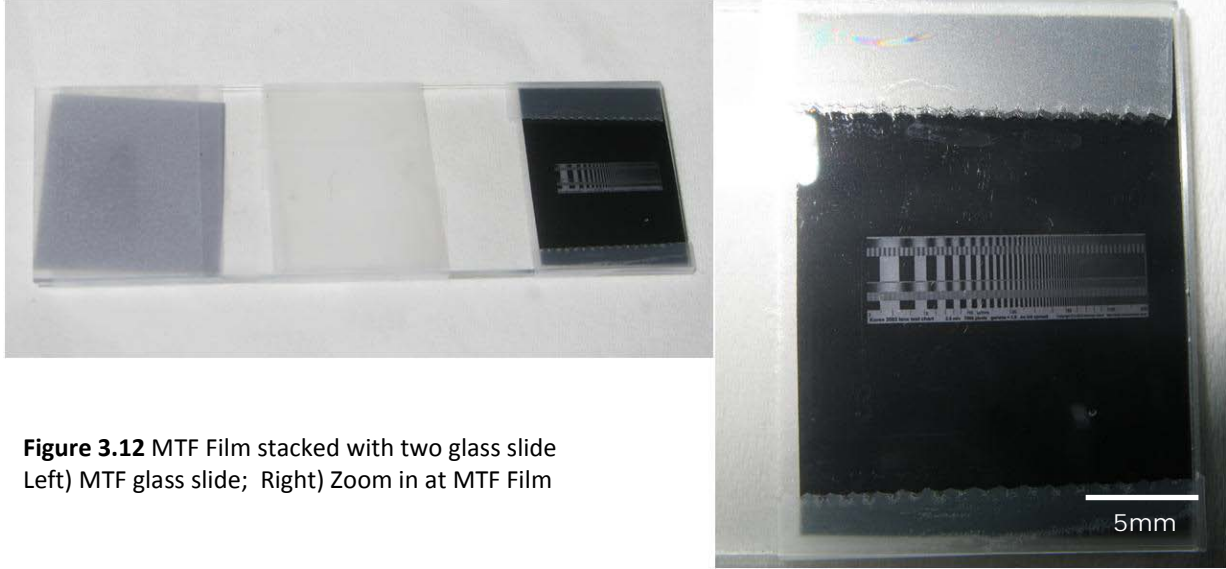
Figure 3.12 MTF Film stacked with two glass slide
Left) MTF glass slide; Right) Zoom in at MTF Film

To distribute the light uniformly, a 3/8 inch frosted glass was placed on the bottom illuminating source. The illuminated MTF film was de-magnified by a 40 times microscope objective lens and projected into the CFB. The MTF chart was transported to the proximal end of the CFB and measured approximately 670µm in length and 210µm in width. Table 1 shows the line pairs/mm ratio. The transported MTF chart has a de-magnification of 3.73 times the original design chart, which means 2 lp/mm on the transported chart actually indicates roughly 7.5 lp/mm in reality.

MTF	Original Chart	Filmed Chart	Transported Chart
Length	2.5mm	12.51mm	.67mm
Lp/mm Ratio	1:1	1:0.20	1:3.73

Table 1 Line pairs ratio for each chart

4.0 Data Analysis

A series of experiments were carried out to identify the LIFDT of the Fujikura FIGH-30-850N CFB. The pulse energy density was increased in sequential steps until the maximum output of the system was reached. Both of the analyses, visual inspection and modulation transfer function, were performed after each transmission to find changes, if any, being made to the CFB.

Visual inspection performed in this experiment is a side-by-side comparison between current and previous images. This technique is used for checking signs of damage such as pits, bubbles, cracks, localized shattering, dead pixel and fused pixels. Modulation transfer function is used for monitoring the change in sharpness or resolution of the CFB. This technique is utilized to check for any newly introduced aberrations of the CFB after each transmission.

4.1   Experimental procedure

To verify whether the CFB was damaged after delivering high energy density pulses, a procedural and systematic routine was followed for taking images for comparison and analysis. Two digital imaging analyses technique were used: 1) visual inspection (VI) and 2) modulation transfer function (MTF).Before and after all experiments a set of images was taken in the sequence list below:

   1. Distal end with top illumination

   2. Distal end with bottom illumination

   3. Proximal end with top illumination

   4. Proximal end with bottom illumination

   5. Proximal end with transported MTF image with top illumination

Each set of images was numbered and compared against the previous set to check for inconsistency. For analysis with visual inspection (performed first), images from 1 to 4 were compared. For analysis on modulation transfer function, image 5 was compared.

4.2   Experiment

The experiments aimed at realizing the LIFDT for the CFB by varying the current (via the Current Regulating Segment) and pulse width (through the 555 Timer) to the Laser, and also the connector spacing between the laser and CFB in a way that the energy pumped into the CFB started from low fluence (0.03 J/cm^2) to relatively high fluence (11 kJ/cm^2).

4.2.1   First Experiment Setup and Result Analysis

The test CFB, which was mounted into FCPC connector, was exposed to the high energy pulses through a ST/FCPC adaptor. However, the physical contact between the CFB and ST mounted delivery fiber caused undesirable surface damages as shown in Figure 4.1. A 0.23 mm spacer was instead placed between the two connectors for eliminating surface scuffs.
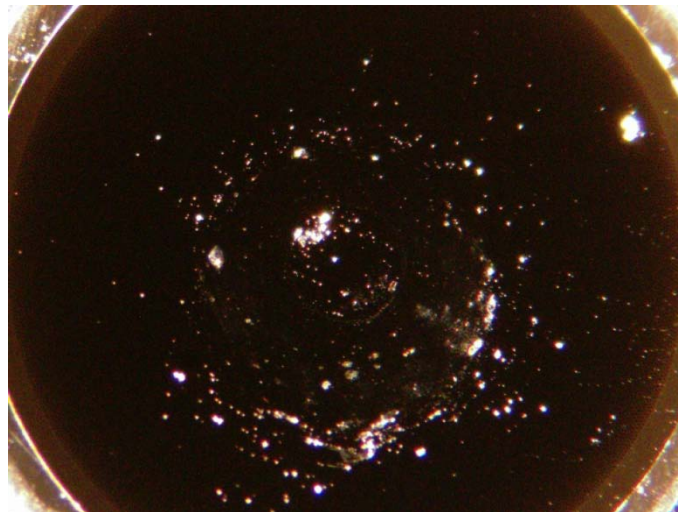
Figure 4.1 Surface Damages on proximal end of CFB caused by
two connectors grinding against each other
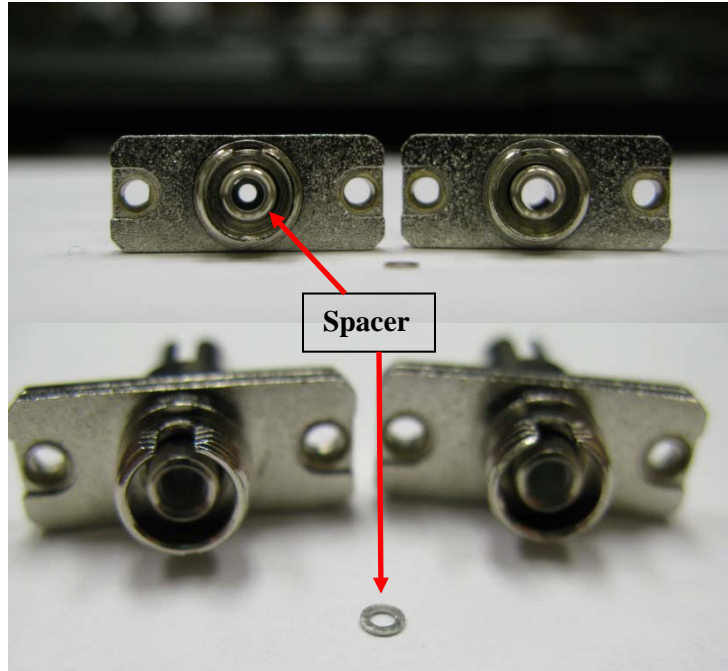
Figure 4.2 The ST/FCPC adaptor on the <u>left</u> is placed with a spacer in the midway of the alignment sleeve. The adaptor on the <u>right</u> is the original ST/FCPC connector. The bottom picture shows the 0.23 mm spacer which was placed inside the adaptor during experiment.

Estimation of the incident energy density on the CFB surface requires knowledge of the spatial distribution at the proximal end of the CFB. Equation (4.1) shows the relationship between the numerical apertures and divergence half-angle, θ.

$$NA = n \sin \theta \qquad (4.1)$$

Since the index of refraction, *n*, for air is approximately 1.0, Equation (4.1) can be rearranged and simplified as Equation (4.2).

$$\theta = \sin^{-1}(NA) \qquad (4.2)$$

Given the numerical aperture, *NA* of the fiber from the laser module is 0.2, the half-angle calculated for the 0.23 mm spacer is approximately 11.54°.

$$\tan \theta = \frac{x}{y} \qquad (4.3)$$

With known parameters, set spacing, y (0.23 mm) and half-angle, θ (11.54°), the new beam diameter formed at the proximal end of the CFB was found to be 143.9 µm.

Table 2 summarizes the experimental conditions necessary to achieve the required range of energy exposures for the CFBs.

	Diameter of Core (cm)		Area of Core (cm^2)	
	0.01439		1.63E-04	
Sequence	Power (mW)	Energy Density per Pulse (J/ cm^2)	Number of Pulse	Total Energy incident on CFB (mJ)
50 ms Pulse Width				
1	0.1	3.07E-02	20	1.00E-01
2	0.1	3.07E-02	200	1.00E+00
3	1	3.07E-01	20	1.00E+00
4	1	3.07E-01	200	1.00E+01
5	10	3.07E+00	20	1.00E+01
6	10	3.07E+00	200	1.00E+02
7	100	3.07E+01	20	1.00E+02
8	100	3.07E+01	200	1.00E+03
9	200	6.15E+01	200	2.00E+03
500 ms Pulse Width				
10	100	3.07E+02	20	1.00E+03
11	100	3.07E+02	200	1.00E+04
12	200	6.15E+02	200	2.00E+04
Full Period Pulse Width				
13	200	1.23E+03	20	4.00E+03
14	200	1.23E+03	200	4.00E+04
15	300	1.84E+03	20	6.00E+03
16	300	1.84E+03	200	6.00E+04

Table 2 Energy density exposed to the CFB from fluence of 0.0307 J/cm^2 to 1840 J/cm^2

<u>Visual Inspection</u>
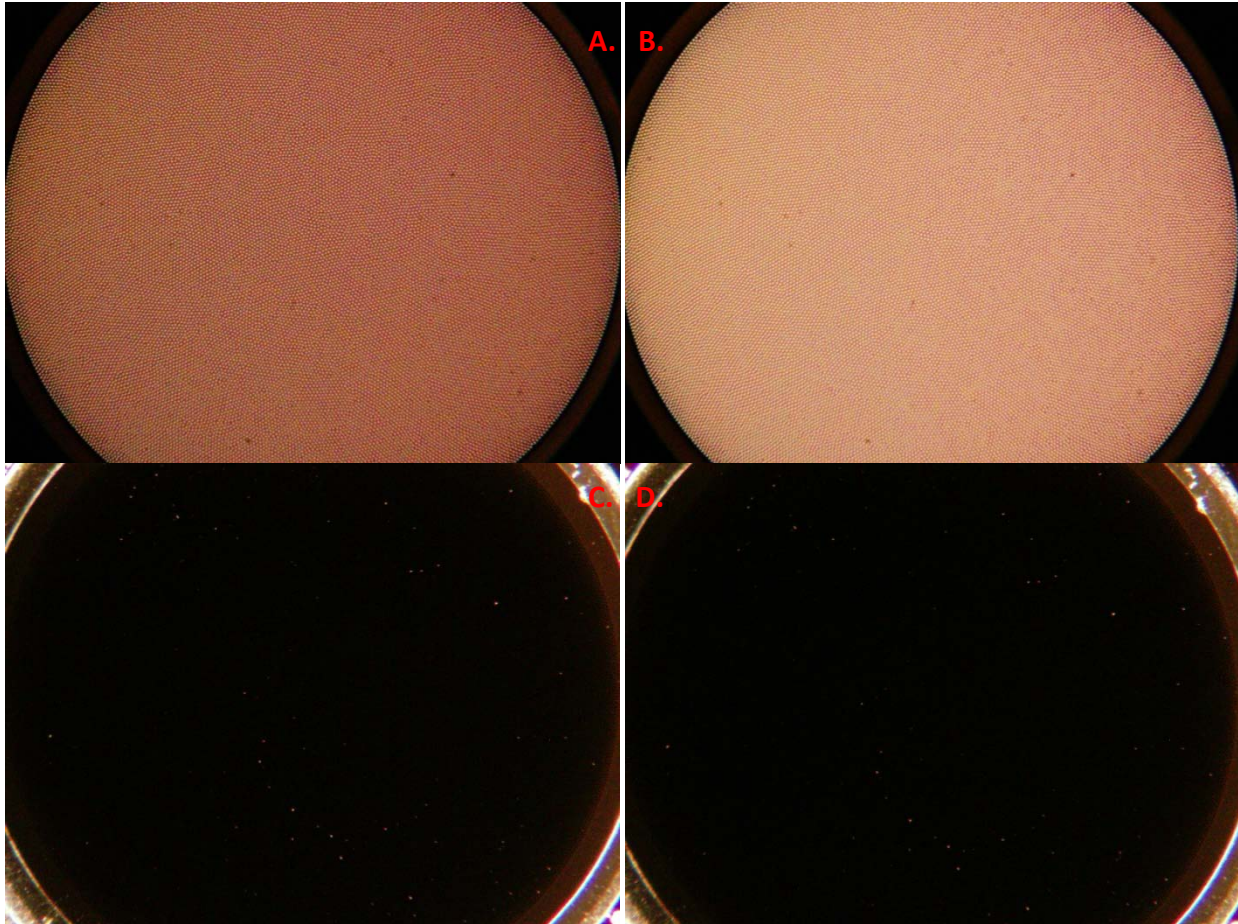
Figure 4.3 Fig. (A) & (C) were images taken at distal end of the CFB before any transmission. Fig. (B) & (D) were the images taken at distal end of the CFB after the last transmission at fluence of 1840 J/cm^2 with duration of 200 second. There is no sign of damage occurred at distal end of the fiber. The black dots appear on the CFB in Fig. (A) & (B) are dust on the camera sensor, and the bright dots on the CFB appear in Fig. (C) & (D) are the leftover residues of metal dust after the CFB was polished.

Beside the images were taken under slightly different illumination intensity from the light source, there appears to be no sign of damage at the distal end of the CFB after sequence of transmissions.
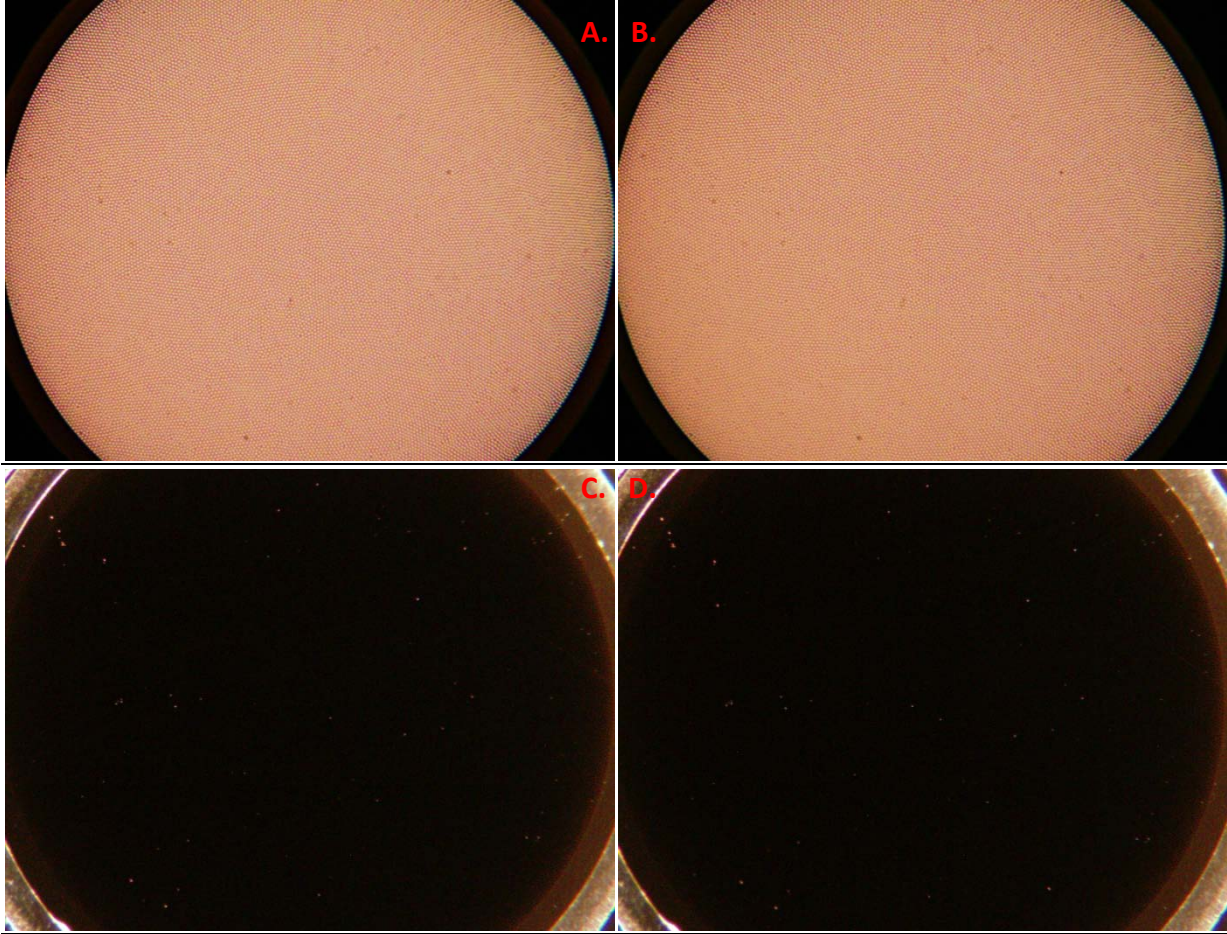
Figure 4.4 Fig. (A) & (C) were images taken at the proximal end of CFB before any transmission. Fig. (B) & (D) were the images taken at the proximal end of CFB after the last transmission at fluence of 1840 J/cm^2 with duration of 200 second. Again, there is no sign of damage occurred at the proximal end of the fiber.

Visual inspection showed no detectable damage on either side of the CFB for the power transmission sequences used. Next, the images were processed through the MTF test to identify if the resolution of the CFB degraded after the transmissions.

Modulation Transfer Function
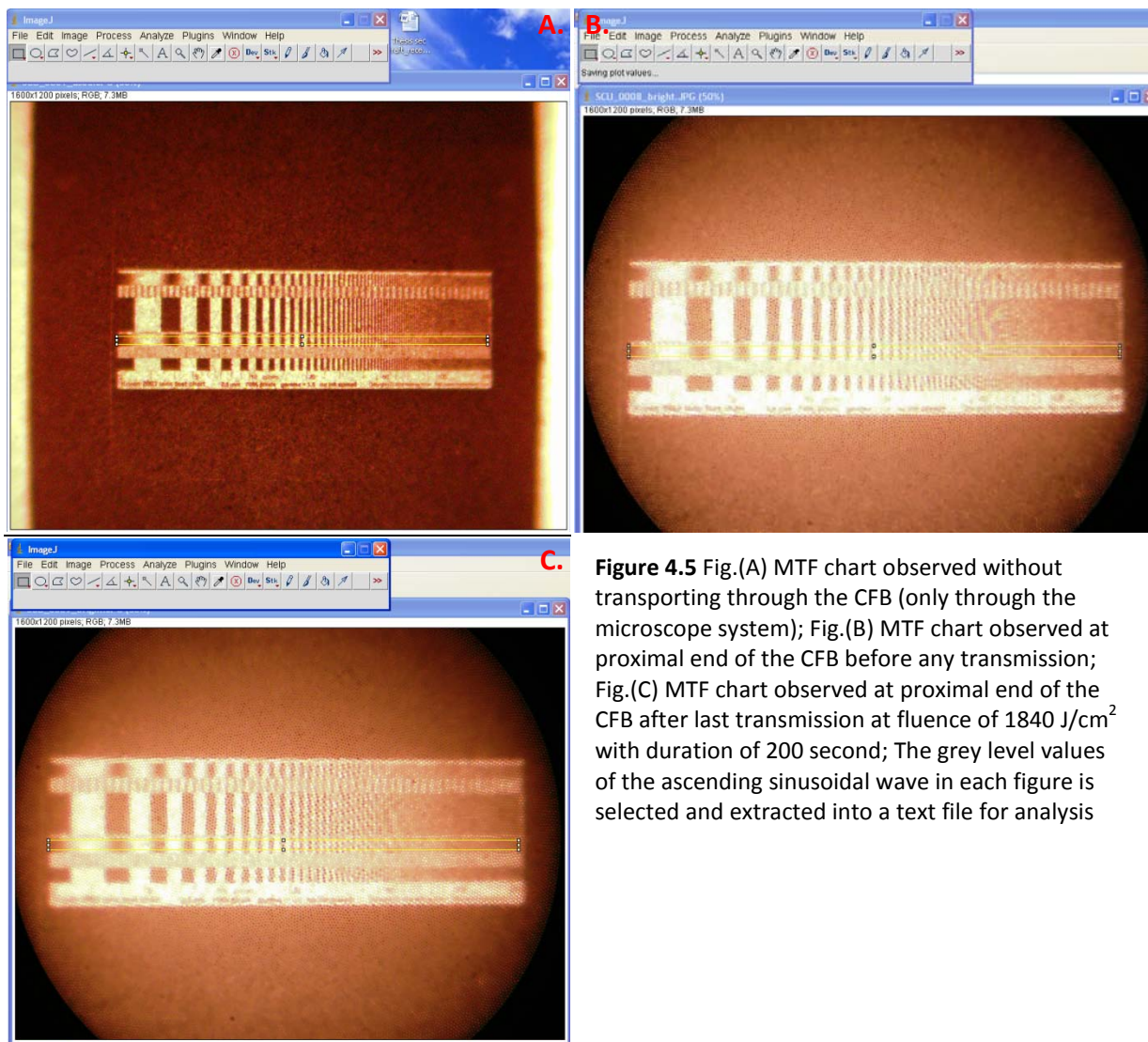
Figure 4.5 Fig.(A) MTF chart observed without transporting through the CFB (only through the microscope system); Fig.(B) MTF chart observed at proximal end of the CFB before any transmission; Fig.(C) MTF chart observed at proximal end of the CFB after last transmission at fluence of 1840 J/cm^2 with duration of 200 second; The grey level values of the ascending sinusoidal wave in each figure is selected and extracted into a text file for analysis

Figure 4.5 displays the slide MTF chart and the transported MTF chart observed at

proximal end of the CFB before and after the last transmission; there is no visible indication of

whether the resolution of the system was altered judging from the bar pattern. For actual MTF

test, the ascending sinusoidal wave in the transported MTF chart for each recorded image was

selected in ImageJ (shown in Figure 4.5) and the gray level values were extracted accordingly

and written into a text file. The text files were imported into MATLAB and processed by a modified version of Norman Koren's sampled code "sfrcalc.m", stands for "spatial frequency response calculation". The modification of the code includes the use of predetermined peak locations extracted from a perfect MTF chart to improve finding the correct peak locations in the captured MTF chart, automatic re-adjustment on the peak location detections when the extracted MTF image is different length and additional shift input parameter for matching the peaks more accurately.

Plots in Figure 4.6 were generated after the sampled code was run for each extracted data set. There are four individual graphs in each plot. The top-most graph (1) is an image of the sinusoidal amplitude grating with varying frequency. The second graph (2) displays grey level values with respect to its pixel locations on the recorded image. The third graph (3) shows the grey level values according to line pairs per millimeter on the x-axis spatial frequency. And the last graph (4) on the bottom of the plot is the derived MTF of the system.

The third graph of each subplot in Figure 4.6 shows the expected reduction in the contrast of the ascending sine waves as the spatial frequency increases. The upper limit of resolution is reached as the contrast approaches zero. Slight magnitude shift in grey level values in different plots were contributed by factors such as minor misalignment of the position of the CFB on the microscope and the fluctuation in illumination intensity at the bottom light source of the microscope.

The fourth graph, MTF of the system under test, is obtained by normalizing the data in the third graph under the assumption that M_o is unity, that is, the ideal object has a contrast of unity at all frequencies. The original MATLAB code "sfrcalc.m" was modified to adapt nosier

captured images (imperfections of the system) by finding the peak values more accurately and thereby obtaining a more reliable and comprehensive MTF graph. A smoothed MTF, red-dotted line, was obtained using a five-point moving average. Due to varying illumination intensity of the light source and auto contrast feature of the camera, each MTF graph had been self-corrected by finding and dividing the maximum value of a modulation index (shown in Equation 2.1) in the system. With assumption of the light source was uniformly distributed, this technique could give an accurate normalization for comparative MTF graphs.
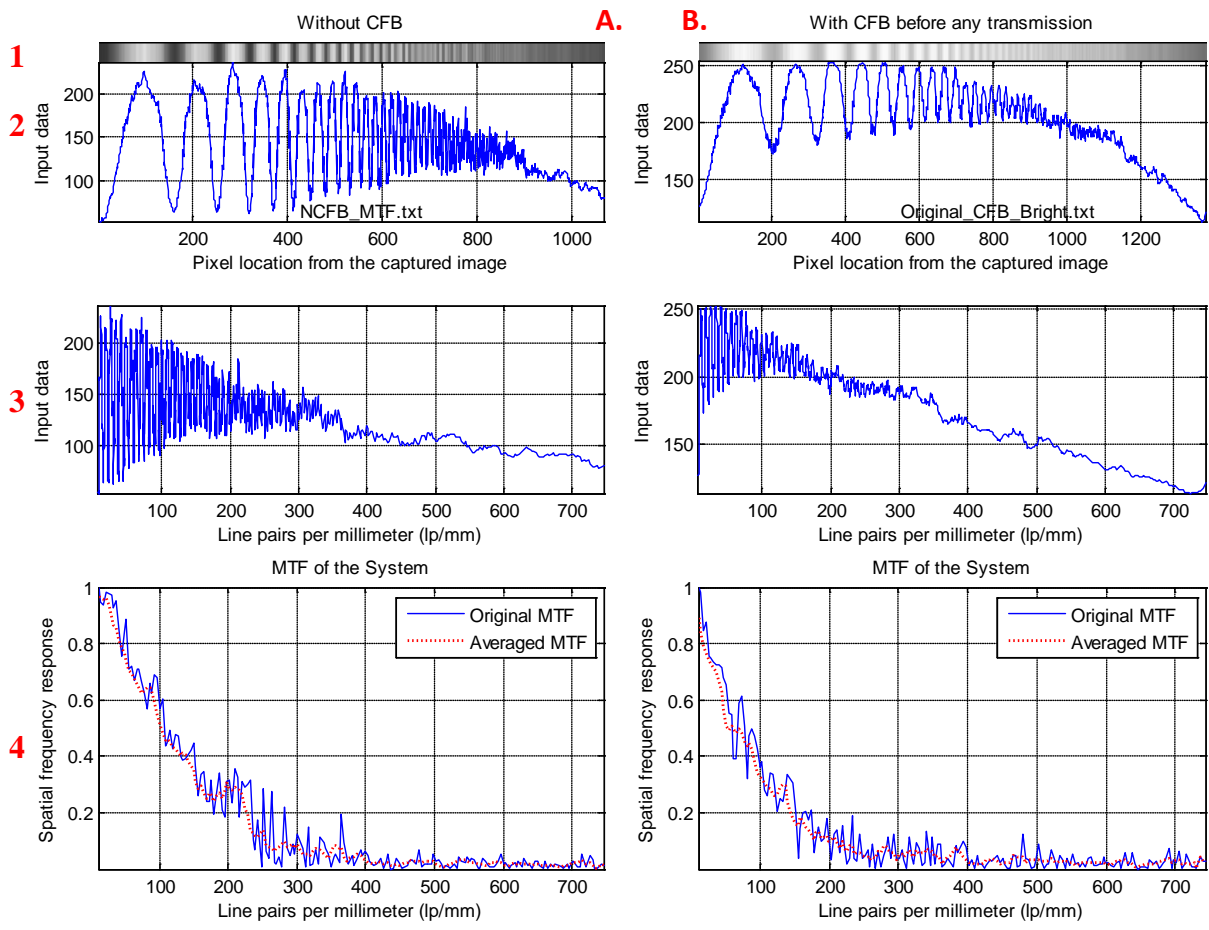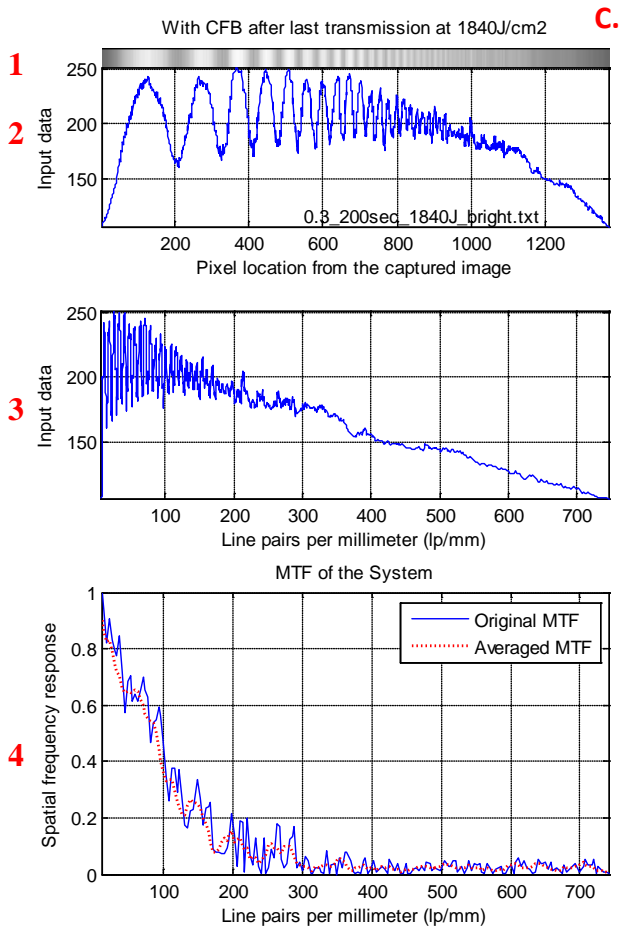
Figure 4.6 MTF comparisons of the system Fig. (A) Illustrates the resolution of the slide MTF chart combined with microscope analysis system. Fig. (B) & (C) were the images taken with the CFB before any transmission and after the last transmission. Graph (1) is the graphic illustration of the captured image. Graph (2) displays grey level values with respect to its pixel locations. Graph (3) shows the grey level values according to line pairs per millimeter. Graph (4) is the derived MTF of the system

From the comparison of the fourth graphs of subplots (A) and (B) in Figure 4.6, the MTF without the CFB is better than the MTF with the CFB. This is mainly due to the resolution of the CFB which is limited by the size of each individual fiber. Comparison of the fourth graphs of subplots (B) and (C) in Figure 4.6 indicates no degradations in resolution of the CFB after series of transmissions with the highest energy density at 1840 J/cm^2 in 200 second duration. The slight variations in MTF curves were due to number of reasons, for example, the minor inconsistence in position of the CFB, not uniformly distributed illumination source and mismatched modulation peaks for each MTF plot.

4.2.2 Second Experiment Setup and Result Analysis

There was no damage identified with previous experiment, therefore, a new spacer with a smaller value, 0.105 mm in thickness, was used to achieve higher energy density. Following the same calculations from Equation (4.1) to (4.3), the new beam diameter was found to be 92.9 µm.

Table 3 illustrates the energy density exposed to same CFB used in previous experiment with the new spacer.

Diameter of Core (cm)			Area of Core (cm^2)	
0.0092866			6.77E-05	
Sequence	Power (mW)	Energy Density per Pulse (J/ cm^2)	Number of Pulse	Total Energy incident on CFB (mJ)
Full Period Pulse Width				
1	200	2.95E+03	20	4.00E+03
2	200	2.95E+03	200	4.00E+04
3	300	4.43E+03	20	6.00E+03
4	300	4.43E+03	200	6.00E+04

Table 3 Energy density exposed to the CFB from fluence of 2950 J/cm^2 to 4430 J/cm^2

Figure 4.7 Fig. (A) and (C) were images taken at the distal end of CFB before any transmission. Fig. (B) and (D) were the images taken at the distal end of CFB after the last transmission at fluence of 4430 J/cm^2 with duration of 200 second. There is no sign of damage occurred at the distal end of the fiber.

Figure 4.8 Fig. (A) & (C) were images taken at the proximal end of CFB before any transmission. Fig. (B) & (D) were the images taken at the proximal end of CFB after the last transmission at fluence of 4430 J/cm^2 with duration of 200 second. Again, there is no sign of damage occurred at the proximal end of the fiber.

Again, visual inspection test shows no detectable difference between the images taken before any transmission and after the last transmission at 4.43 kJ/cm^2 on both end of the CFB.

Modulation Transfer Function
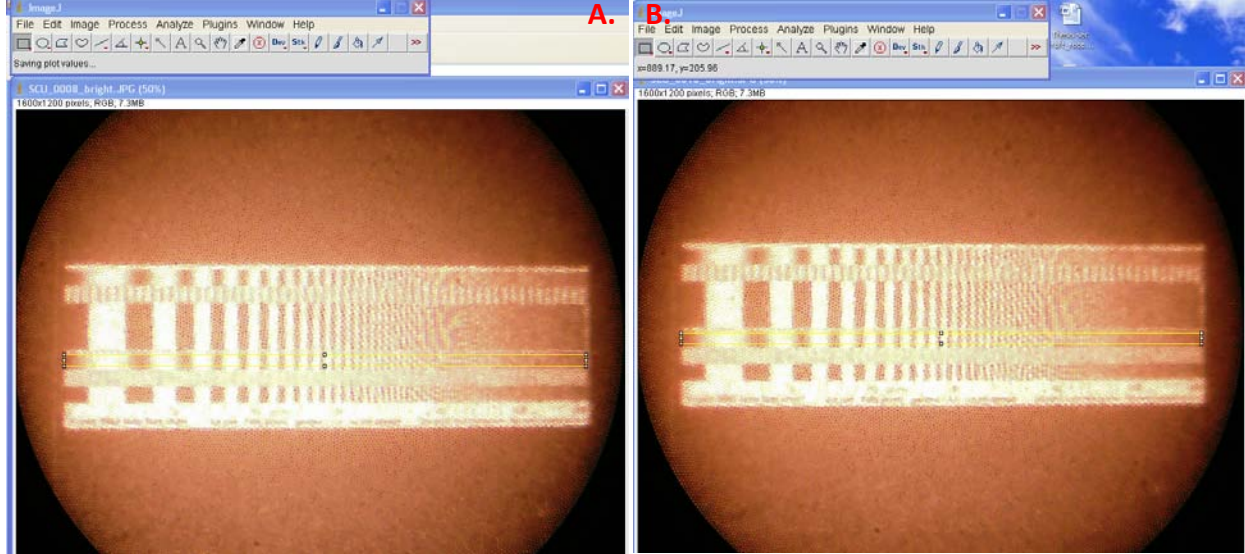
Figure 4.9 Fig.(A) MTF chart observed at proximal end of the CFB before any transmission; Fig.(B) MTF chart observed at proximal end of the CFB after last transmission at fluence of 4430 J/cm^2 with duration of 200 second;
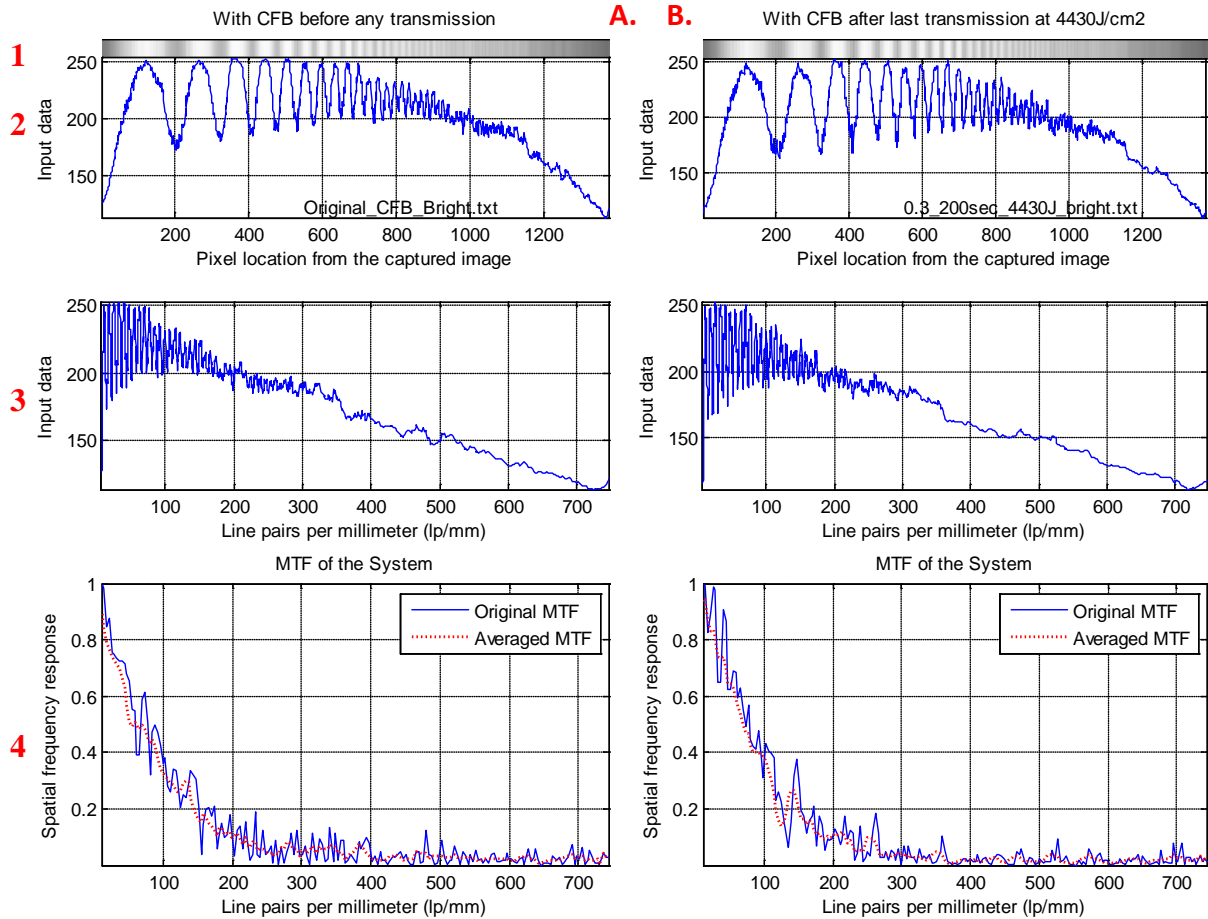
Figure 4.10 Fig. (A) was a image taken with CFB before any transmission; Fig. (B) was a image taken after last transmission at 4430 J/cm^2 with duration of 200 second;

The differences in the magnitude of contrast of the ascending sine waves in third graphs of Figure 4.10 were caused by small variation in alignment of the CFB on the microscope and changes in illumination intensity of the light source as described before.

In comparison of the fourth graphs in Figure 4.10, the MTF exhibits no indicative changes to the resolution of CFB before and after transmitting series of continuous high energy density laser signals. With the highest setting reaching at 4430 J/cm^2 in 200 second duration, the CFB was remained unaffected by the output of the laser. Due to system limitations, the energy density of the existing laser module could not be increased further.

4.2.3 Third Experiment Setup and Result Analysis

A new laser with higher energy density became available during our investigation. This laser module is well documented and came with a built-in power adjustment and current detecting circuits. It was designed and fabricated by JDS Uniphase (JDSU) Corporation with CW output power up to 2 Watt at 830 nm. The laser diode, 2486-L4 series, is pigtailed with a 1 meter long, 0.22 NA, 60/125 µm core fibers and terminated in a FCPC connector.

The laser was driven by a two ampere current source for one watt of output power. The two previous spacers were used to obtain a range of higher energy densities as depicted in Table 4.

.23mm Spacer				
Diameter of Core (cm)			Area of Core (cm^2)	
0.016374169			2.11E-04	
Sequence	Power (mW)	Energy Density per Pulse (J/ cm^2)	Number of Pulse	Total Energy incident on CFB (mJ)
Full Period Pulse Width				
1	1000	4.75E+03	20	2.00E+04
2	1000	4.75E+03	200	2.00E+05
.105mm Spacer				
Diameter of Core (cm)			Area of Core (cm^2)	
0.010736033			9.05E-05	
Sequence	Power (mW)	Energy Density per Pulse (J/ cm^2)	Number of Pulse	Total Energy incident on CFB (mJ)
Full Period Pulse Width				
3	1000	1.10E+04	20	2.00E+04
4	1000	1.10E+04	200	2.00E+05

Table 4 Energy density exposed to the CFB from fluence of 4750 J/cm^2 to 11000 J/cm^2

The same CFB from previous experiments was reused with the new laser for consistency. Due to some dust collected on the proximal end of the CFB, this side of the CFB had been re-polished to remove particles which might affect the result of our experiment.
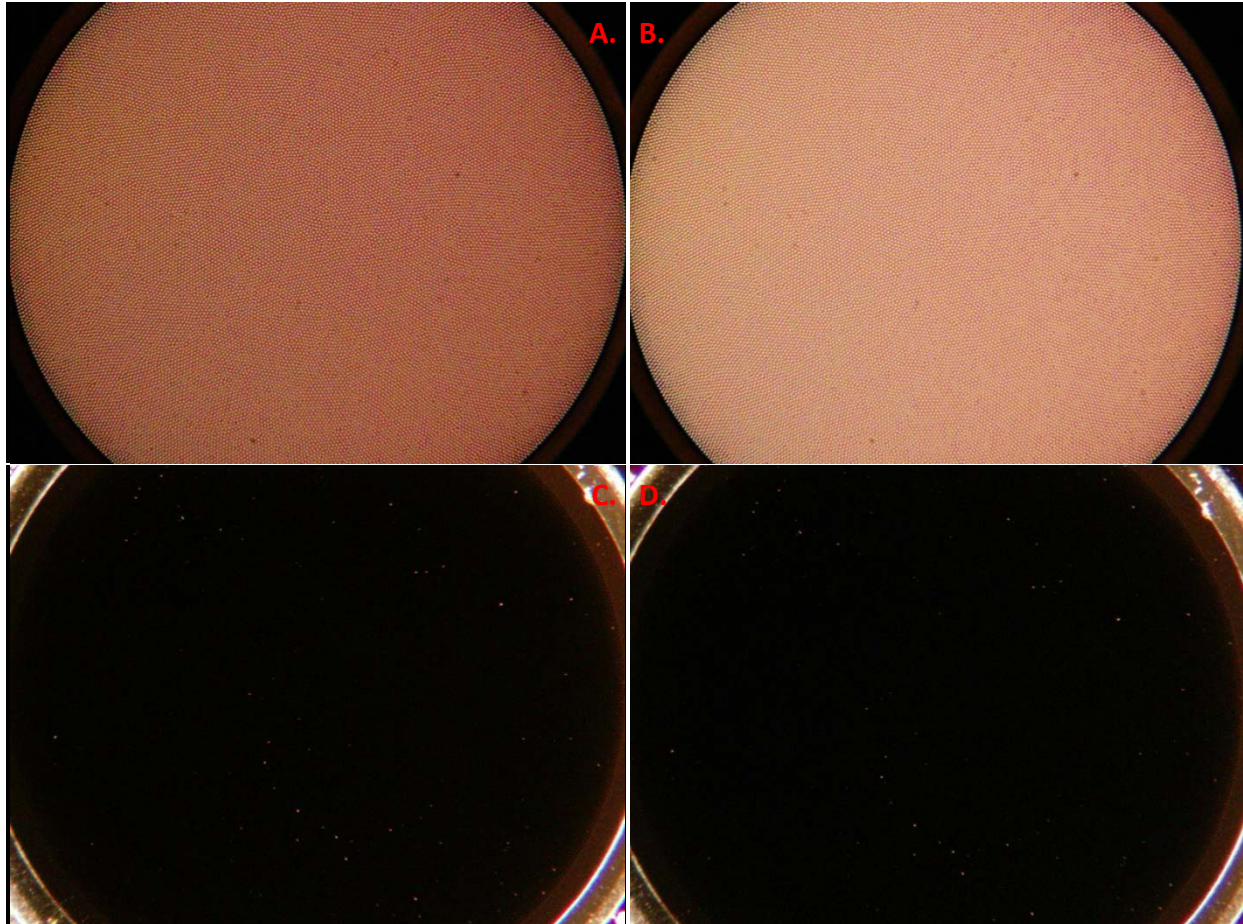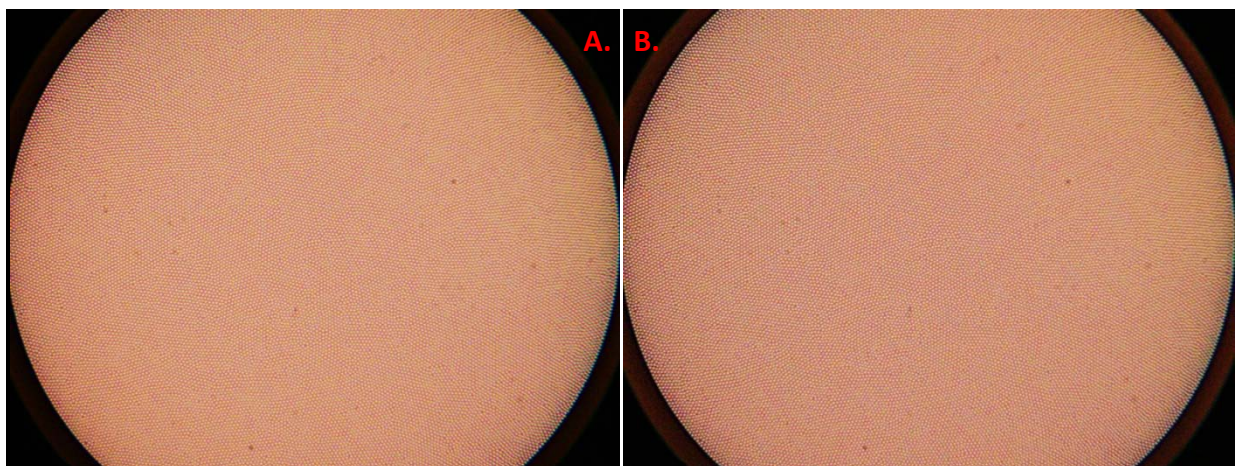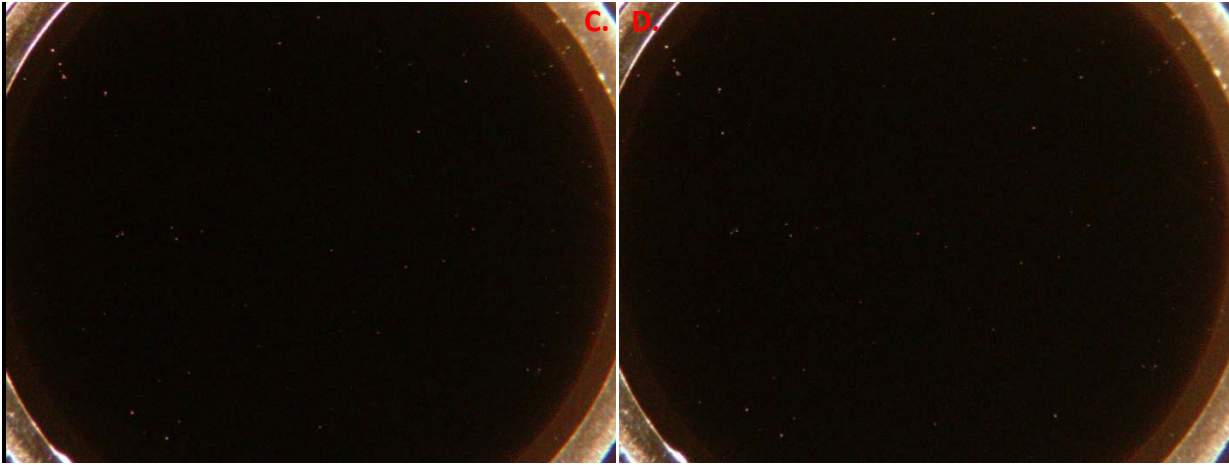
Visual Inspection
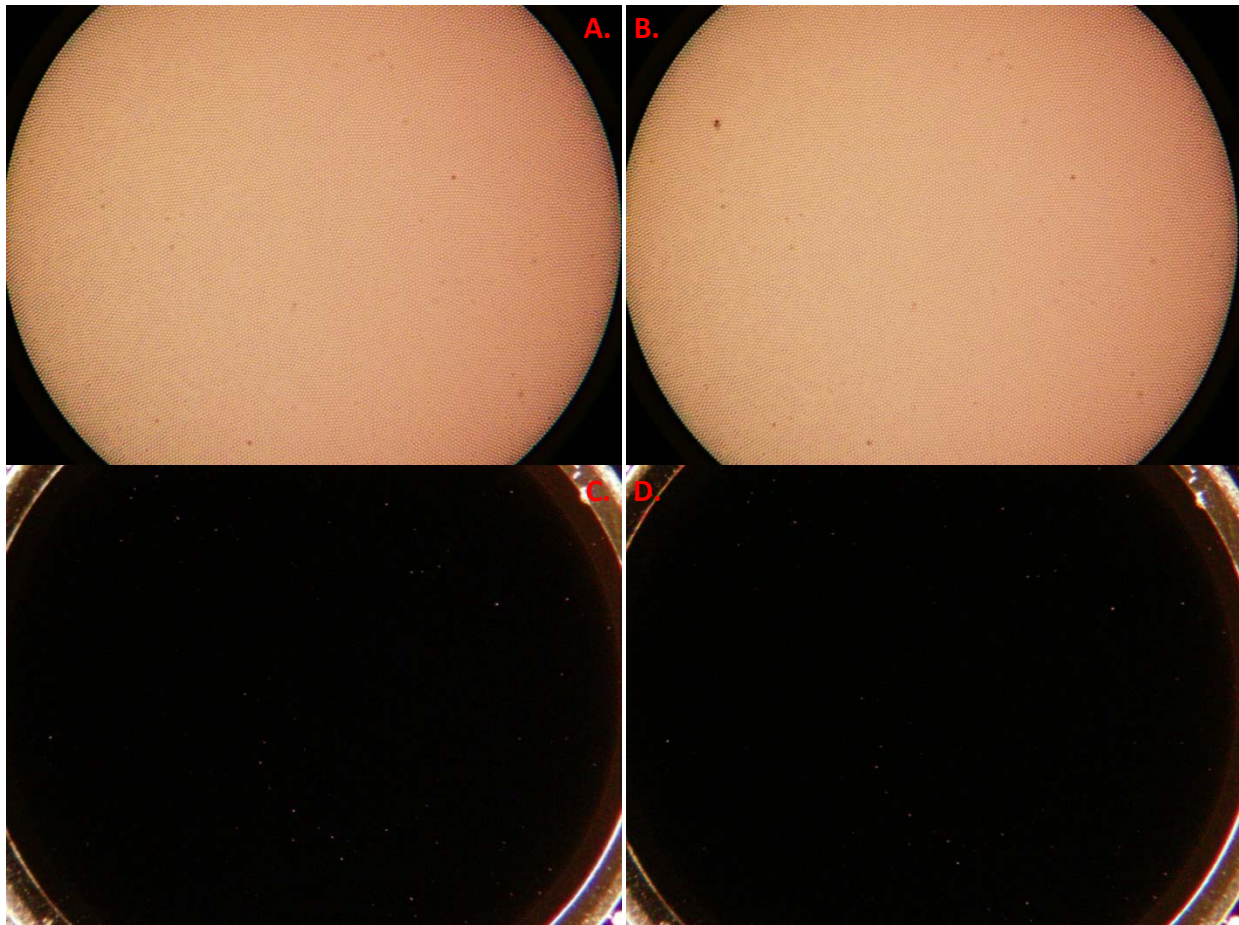
Figure 4.11 Fig.(A) and (C) were images taken at the distal end of CFB before any transmission. Fig.(B) and (D) were the images taken at the distal end of CFB after the last transmission at fluence of 11 kJ/cm^2 with duration of 200 second. The dark spots in Fig.(B) appear to formed at proximal end of the CFB was identified as dust, not actual damaged.
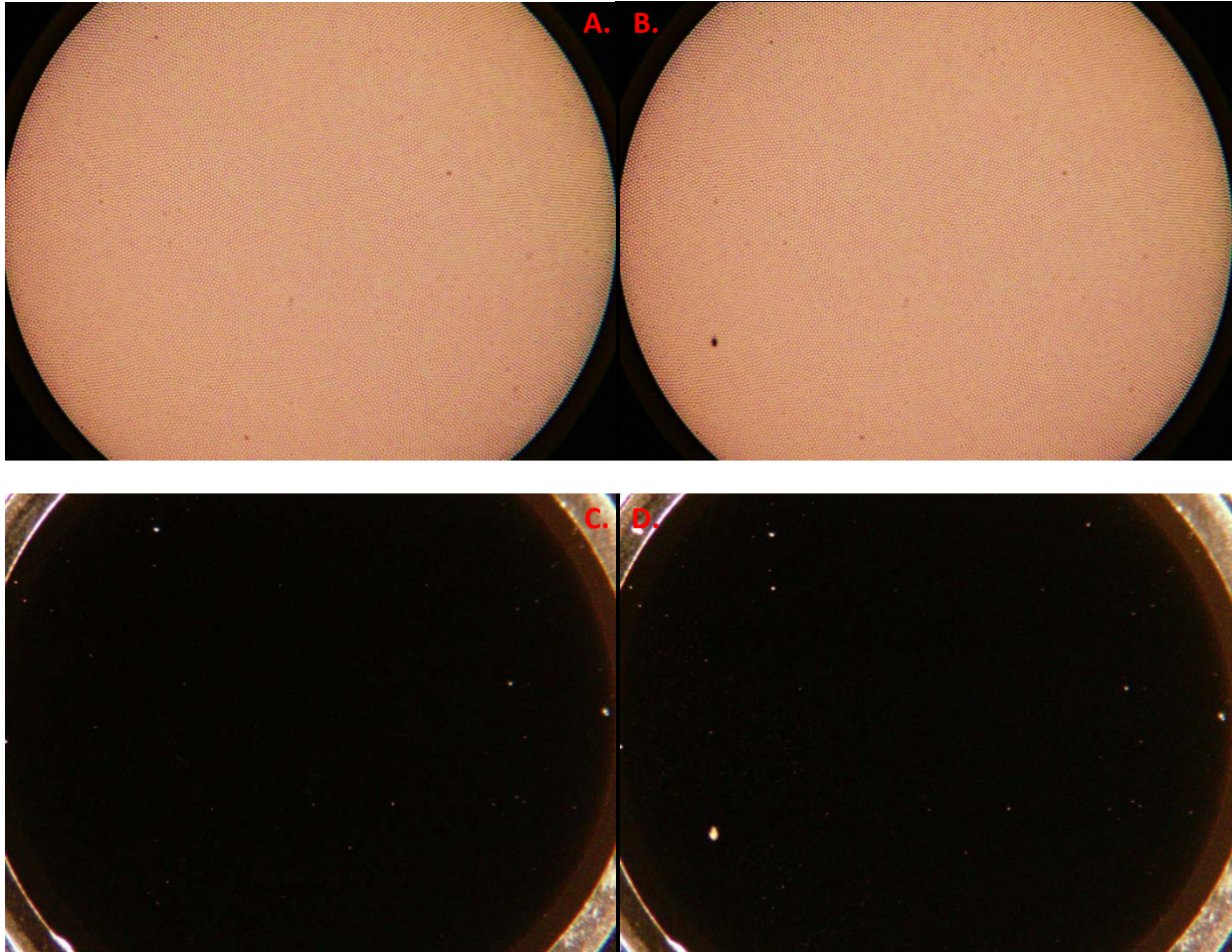
Figure 4.12 Fig.(A) & (C) were images taken at the proximal end of the re-polished CFB before any transmission. Fig.(B) & (D) were the images taken at the proximal end of the re-polished CFB after the last transmission at fluence of 11 kJ/cm^2 with duration of 200 second. The dark spots at Fig.(B) or bright spots at Fig.(D) appear to be some sort of metallic dust and not actual damage to the fiber (the dust appeared after the first transmission).

There were some metallic particles introduced during the first transmission in our experiment. This is believed happened during the initial connecting process of jointing two connectors into the new FCPC/FCPC adopter. However, these particles did not appear to affect the performance nor introduced damages (pits) after series of high power laser transmissions to the CFB; there is no visible damage to the fiber besides observing these particles.

Modulation Transfer Function
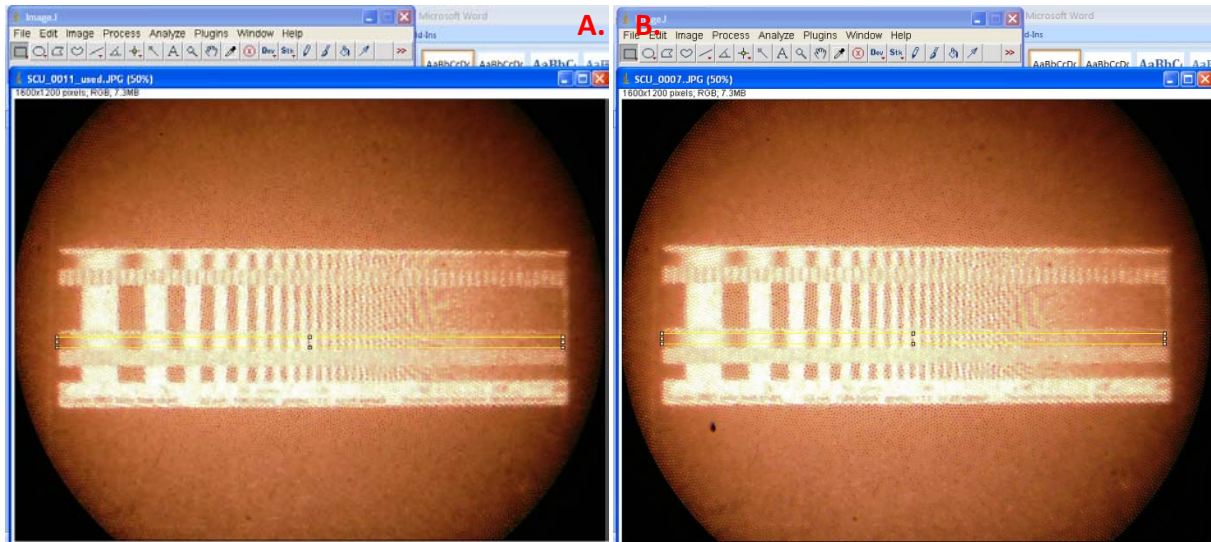
Figure 4.13 Fig.(A) MTF chart observed at proximal end of the re-polished CFB before any transmission; Fig.(B) MTF chart observed at proximal end of the re-polished CFB after last transmission at fluence of 11000 J/cm² with duration of 200 second;
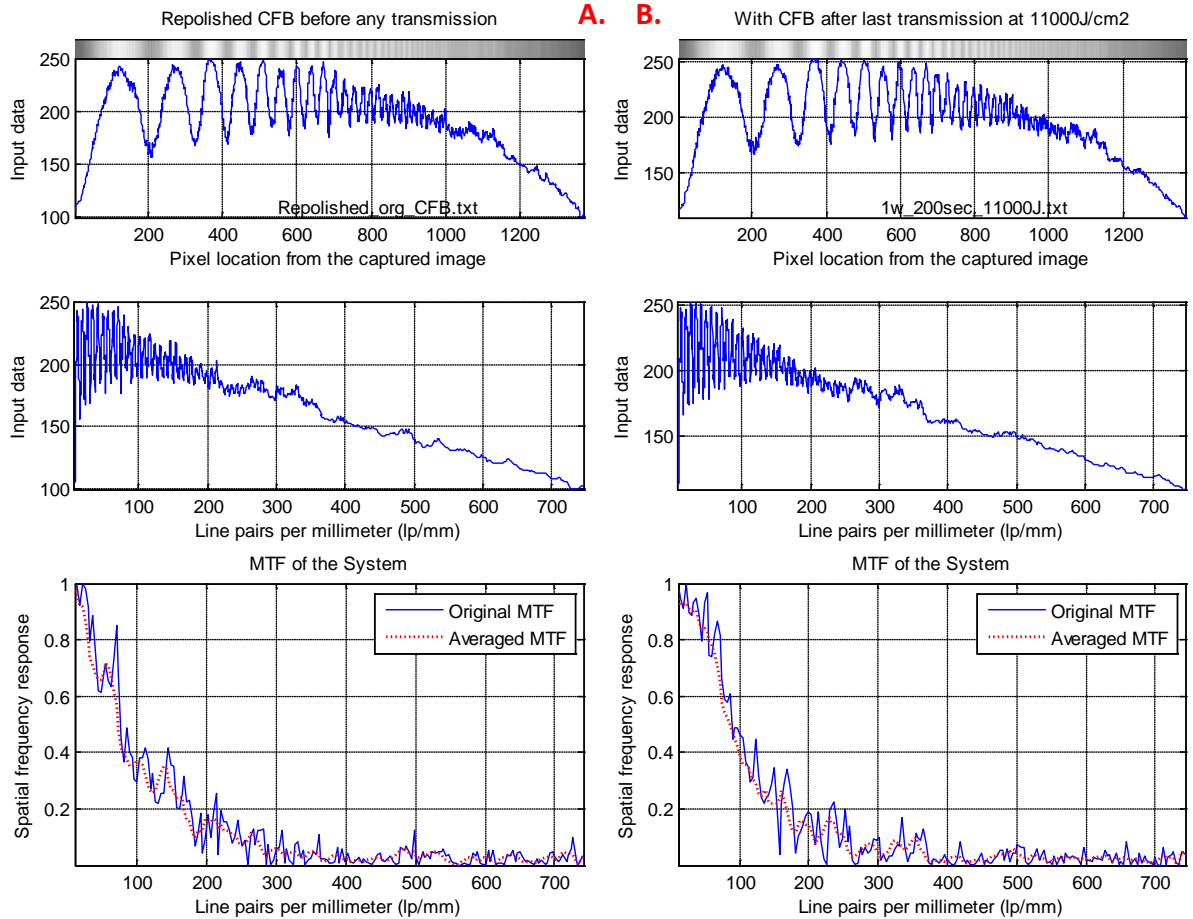
Figure 4.14 Fig.(A) is the MTF before any transmission transported through the repolished CFB; Fig.(B) is the MTF transported through the CFB after the last transmission at fluence of 11000 J/cm^2; there is no degradation in resolution after series of transmissions.

Even with the energy density of the laser reaching 11kJ/cm^2 transmitted through the CFB in CW mode for a duration of 200 second, no image distortion was observed and characteristic changes in MTF was not measurable. This concludes the LIFDT of the CFB at a wavelength in 830 nm regions is beyond 11kJ/cm^2.

4.3 Spot Size Analysis

In previous experiments we have determined the LIFDT is higher than 11kJ/cm^2 which is more than sufficient for any hair removal applications. Now, we want to verify two important characteristics of the CFB for transporting high energy density therapeutic light. First, during the transportation of the laser light, does the incident beam spot size match the exit beam spot size of the CFB? Second, does the beam spot size vary at the distal end of the CFB with respect to changes of the incident energy density? If the beam spot size becomes larger as the laser power increases, it would mostly likely be caused by the laser light leaking into neighboring fibers in the CFB. In either scenario, the output energy density will not be equal to the input energy density; therefore, an equation will have to be derived to approximate the relationship between the input and the output energy densities.

Experiments were performed to address the above questions regarding the CFB's output characteristics. The 0.3 watt fiber laser was set to operate at low (7.8 µW) and high (97mW) power levels for comparing the beam spot sizes at the different energy densities. The exiting beam was captured by a scanning slit beam profiler manufactured from Merchantek Inc. (Merchantec PC-BeamScope) which was placed at distal end of the CFB to measure the diameter of the beam spot during experiment. Due to the location of the beam profiler, a 5 meter 62.5/125 multimode extension fiber was used. A 0.105mm spacer was placed between the multimode extension fiber and the CFB to avoid any superficial damage. The minimal spot size exiting from the distal end of the CFB was calculated to be 122.5 µm.

The first experiment was performed by placing the distal end of the CFB less than 2mm away from the beam profiler. The result obtained (shown in figure 4.15) suggest there was no significant difference in the FWHM between the two energy density.
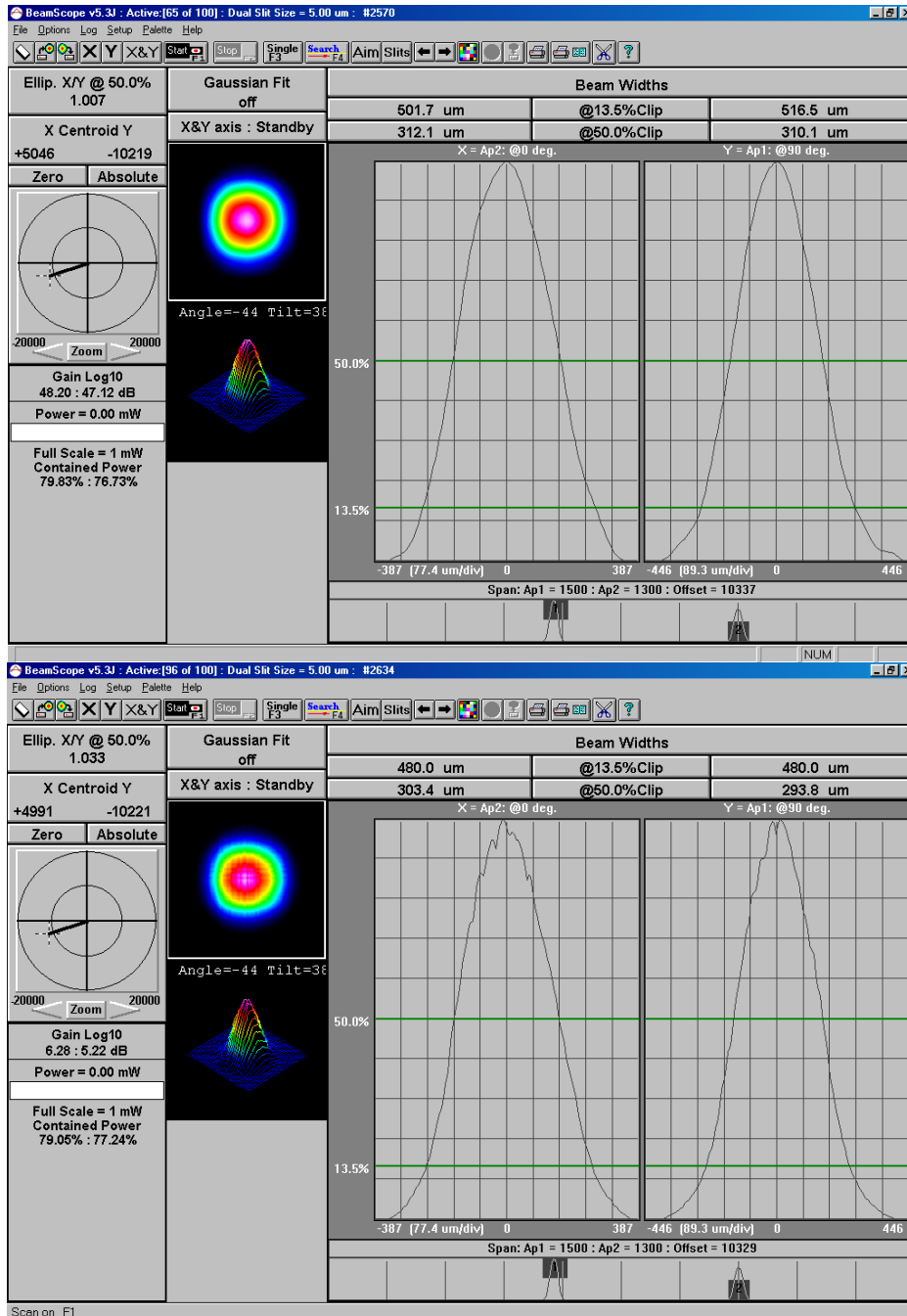
Figure 4.15 The captured beam diameter at distal end of CFB in relatively close (less than 2mm) position to the beam profiler slit with power coupled through a 62.5 Multi-mode fiber at (top) low power setting at 7.8μW and (bottom) high power setting at 97 mW.

The second experiment was performed by placing the distal end of the CFB less than 0.5 mm away from the beam profiler.
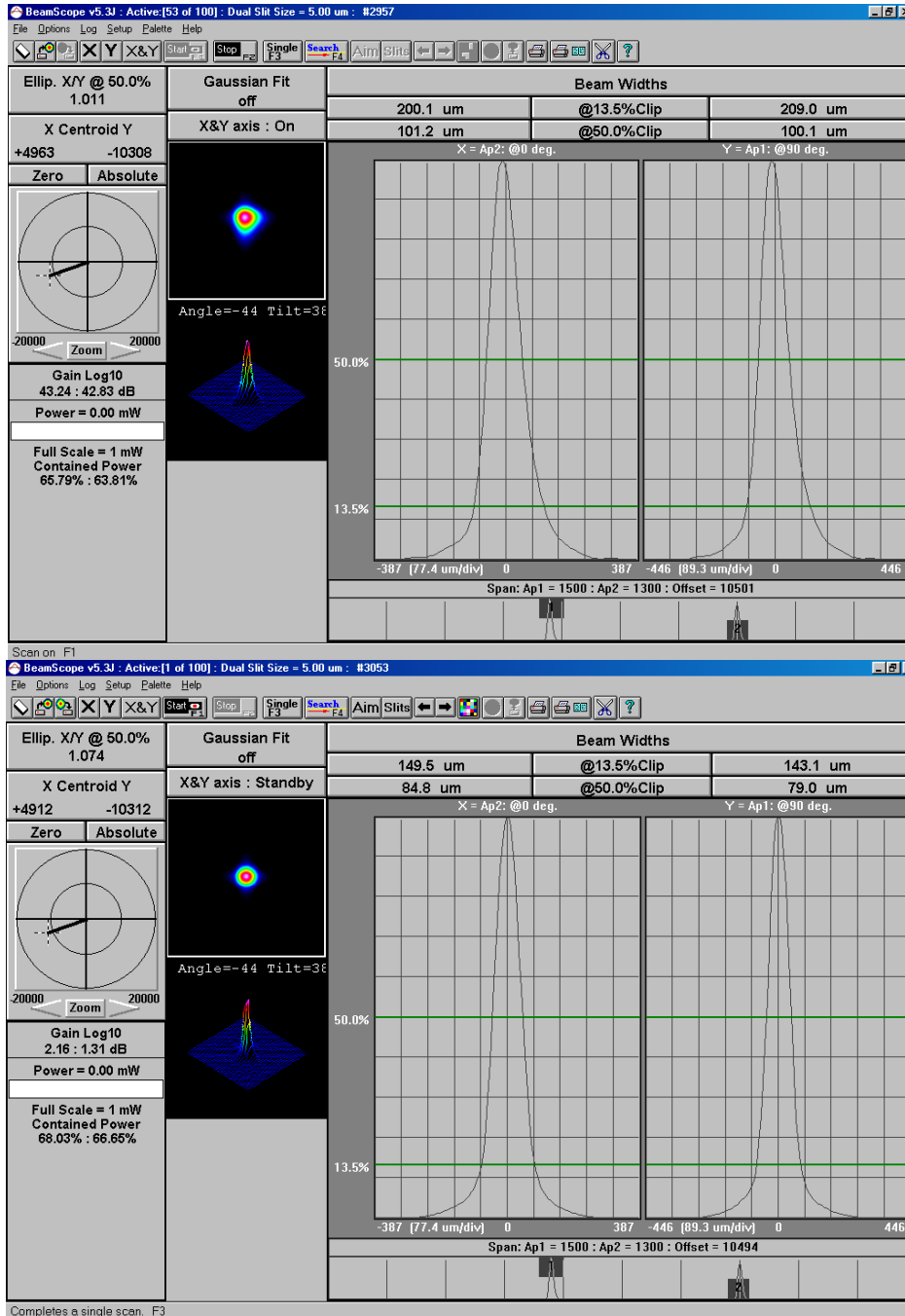
Figure 4.16 The captured beam diameter at the distal end of CFB in extremely close (less than 0.5mm) position to the beam profiler slit with power coupled through a 62.5 Multi-mode fiber at (top) low power setting at 7.8µW and (bottom) high power setting at 97 mW.

The results indicate that the CFB produces a lens-like focusing when the laser output power is high. A 20% reduction in the spot size, close to the CFB surface, was measured. We suspect that the high optical power in the centrally located imaging fibers (2µm in diameter) produce a small increase in the reflective index due to the resulting non-linearity. Subsequently, the CFB behaves like a gradient index fiber lens at the high power setting. This effect is beneficial for the phototherapeutic application discussed in the thesis.

At the low power setting the results were as expected and no measurable change in the spot size was observed. The cross-talk between neighboring fiber elements was negligible as no increase in spot size was observed.

5.0 Conclusions

We have found that a coherent fiber bundle (CFB) can be used for both image transport and delivery of high energy pulses for phototherapeutic applications. Our experiments show that the laser induced damage threshold for the Fujikura FIGH-30-850N is beyond 11 kJ/cm^2. Furthermore, the MTF of the CFB, after exposure to these high energy pulses, remains unchanged, that is, the image quality of the CFB is uncompromised.

Another interesting finding was that a CFB behaves like a gradient index lens at high power levels (approximately 100 mW range). This property can significantly enhance the energy density at the distal end without requiring higher power lasers.

The promising characteristics of the CFB allow us to look further into realizing the compact photoepilation system. In the final product, unlike any conventional system, we would like to utilize the live video feed transported by CFB to achieve semi to full automatic power control. In area of laser hair removal applications, this self-correcting power control feature could eventually evolve to eliminate the need for trained physicians and a leap to further reduce risk of complications after procedure.

Reference

[1] Dwarka N. Bose, "Narinder Singh Kapany – a pioneer in fibre optics", Current Science, Vol. 98, No. 6, 25 March 2010.

[2] Harbans S. Dhadwal, "Patent application title: Coherent imaging fiber based hair removal device".

[3] Jeff Hecht, *Understanding Fiber Optics*, *5th Ed*. (Prentice Hall, April 2005).

[4] Abraham Katzir, "Laser & Optical fibers in medicine", Optics & Photonics News, February 1991.

[5] Warren J. Smith, *Modern Optical Engineering, 3rd Ed*. (SPIE Press, August 2000).

[6] Hytek Microsystems, HY-5610 TEC Controller: Subminiature Controller for Thermoelectric Coolers, November 1997.

[7] H.H. Zenzie and G.B. Altshuler, "Super Long Pulse Hair Removal", 0-7803-5947-X/00 IEEE, 2000.

[8] José L. Lázaro, Pedro R. Fernández, Alfredo Gardel, Ángel E. Cano and Carlos A. Luna, "Sensor calibration based on incoherent optical fiber bundles (IOFB) used for remote image transmission", ISSN 1424-8220. 9, 8215-8229; doi:10.3390/s91008215. Sensor, 2009.

[9] Darryl Shaw Hodson, MD, LTC, "Current and future trends in home Laser devices", Seminar Cutaneous Medicine and Surgery 27: 292-300, Elsevier Inc., 2008.

[10] Norman Koren, "Understanding image sharpness part 5: Lens testing", http://www.normankoren.com/Tutorials/MTF5.html.

[11] Kristen Lantz Reichenbach and Chris Xu, "Analysis and measurement of light prorogation in coherent fiber bundles", OSA 1-55752-834-9, Optical Society of America, 2007.

Appendix A

Thermistor Resistance versus Temperature Chart

°C	R Val (Ω)	°C	R Val (Ω)	°C	R Val (Ω)	°C	R Val (Ω)	°C	R Val (Ω)
-80	7,296,874	-30	176,683	20	12,493.70	70	1,751.60	120	388.59
-79	6,677,205	-29	166,091	21	11,943.30	71	1,693.00	121	378.44
-78	6,114,311	-28	156,199	22	11,420.00	72	1,636.63	122	368.59
-77	5,602,677	-27	146,959	23	10,922.70	73	1,582.41	123	359.05
-76	5,137,343	-26	138,322	24	10,449.90	74	1,530.28	124	349.79
-75	4,713,762	-25	130,243	25	10,000.00	75	1,480.12	125	340.82
-74	4,327,977	-24	122,687	26	9,572.00	76	1,431.87	126	332.11
-73	3,966,352	-23	115,613	27	9,164.70	77	1,385.37	127	323.67
-72	3,655,631	-22	108,991	28	8,777.00	78	1,340.68	128	315.48
-71	3,362,963	-21	102,787	29	8,407.70	79	1,297.64	129	307.53
-70	3,095,611	-20	96,974	30	8,056.00	80	1,256.17	130	299.82
-69	2,851,363	-19	91,525	31	7,720.90	81	1,216.23	131	292.34
-68	2,627,981	-18	86,415	32	7,401.70	82	1,177.75	132	285.08
-67	2,423,519	-17	81,621	33	7,097.20	83	1,140.71	133	278.03
-66	2,236,398	-16	77,121	34	6,807.00	84	1,104.99	134	271.19
-65	2,064,919	-15	72,895	35	6,530.10	85	1,070.58	135	264.54
-64	1,907,728	-14	68,927	36	6,266.10	86	1,037.40	136	258.09
-63	1,763,539	-13	65,198	37	6,014.20	87	1,005.40	137	251.82
-62	1,631,173	-12	61,693	38	5,773.70	88	974.56	138	245.74
-61	1,509,639	-11	58,397	39	5,544.10	89	944.81	139	239.82
-60	1,397,935	-10	55,298	40	5,324.90	90	916.11	140	234.08
-59	1,295,239	-9	52,380	41	5,115.60	91	888.41	141	228.50
-58	1,200,732	-8	49,633	42	4,915.50	92	861.70	142	223.08
-57	1,113,744	-7	47,047	43	4,724.30	93	835.93	143	217.80
-56	1,033,619	-6	44,610	44	4,541.60	94	811.03	144	212.68
-55	959,789	-5	42,314.60	45	4,366.90	95	786.99	145	207.70
-54	891,689	-4	40,149.50	46	4,199.90	96	763.79	146	202.86
-53	828,865	-3	38,108.50	47	4,040.10	97	741.38	147	198.15
-52	770,880	-2	36,182.80	48	3,887.20	98	719.74	148	193.57
-51	717,310	-1	34,366.10	49	3,741.10	99	698.82	149	189.12
-50	667,828	0	32,650.80	50	3,601.00	100	678.63	150	184.79
-49	622,055	1	31,030.40	51	3,466.90	101	659.10		
-48	579,718	2	29,500.10	52	3,338.60	102	640.23		
-47	540,530	3	28,054.20	53	3,215.60	103	622.00		
-46	504,230	4	26,687.60	54	3,097.90	104	604.36		
-45	470,609	5	25,395.50	55	2,985.10	105	587.31		
-44	439,445	6	24,172.70	56	2,876.90	106	570.82		
-43	410,532	7	23,016.00	57	2,773.20	107	554.86		
-42	383,712	8	21,921.70	58	2,673.90	108	539.44		
-41	358,806	9	20,885.20	59	2,578.50	109	524.51		
-40	335,671	10	19,903.50	60	2,487.10	110	510.06		
-39	314,179	11	18,973.60	61	2,399.40	111	496.08		
-38	294,193	12	18,092.60	62	2,315.20	112	482.55		
-37	275,605	13	17,257.40	63	2,234.70	113	469.45		
-36	258,307	14	16,465.10	64	2,156.70	114	456.76		
-35	242,195	15	15,714.00	65	2,082.30	115	444.48		
-34	227,196	16	15,001.20	66	2,010.80	116	432.58		
-33	213,219	17	14,324.60	67	1,942.10	117	421.06		
-32	200,184	18	13,682.60	68	1,876.00	118	409.90		
-31	188,026	19	13,052.80	69	1,812.60	119	399.08		